MSci RHUL Physics Major Project

SEARCHING FOR AXIONS IN THE DEAP-3600 DETECTOR

March 13, 2017

Abstract

A method was developed to search for axions and axion-like-particles interacting in the DEAP-3600 liquid argon detector via the axio-electric effect. The analysis strategy is to look for bumps in the measured electron spectrum, and use this to set a constraint on the axion coupling versus axion mass. This will be the first axion search in a liquid argon detector. It could potentially increase the sensitivity by a factor of 100 over published results due to the large size of the DEAP-3600 target mass compared with other experiments.

Hannah M. Wakeling
Supervised by Prof. J. Monroe and Dr. J. Walding

Contents

1 Introduction

Axions are pseudoscalar Nambu-Goldstone bosons that are theorised as extensions to the Standard Model (SM). They are motivated to solve the strong Charge-Parity (CP) problem of Quantum Chromodynamics (QCD) via a breaking of a global $U(1)$ symmetry [1]. After the axion was hypothesised, the axion-like-particle (ALP) was postulated. The ALP does not necessarily solve the strong CP problem, but still has the pseudoscalar properties of the axion. If an axion or ALP is a Nambu-Goldstone boson it is predicted to have a coupling to matter that is less than the weak interaction coupling strength; the implication here is that axions or ALPs are natural dark matter (DM) candidates [2].

The source of axions and ALPs is hypothesised to be the DM halo of our own galaxy and thermal production within stellar objects. Section 2 reviews axion and ALP production mechanisms, current constraints, and direct detection methods. Section 3 describes the DEAP-3600 detector and how it identifies events. The axion search and other electron-like events within the detector backgrounds are then discussed with background mitigation methods. Section 4 develops a method to search for axions and ALPs in DEAP-3600. This method is applied to search for solar axions between 1 and 14 keV.

2 Axion and ALP detection

This section first reviews the theory and properties of axions and ALPs in Section 2.1. Their cosmological and astrophysical constraints are then inspected in Section 2.2. Finally direct detection methods of axions and ALPs are examined in Section 2.3 and current experimental constraints are compared.

2.1 Axions and ALPs

Axions and ALPs are defined by three main parameters: their mass m_A, their couplings g_A and their energy scale or "decay constant" f_A. The axion mass m_A and axion-photon couplings $g_{A\gamma}$ are proportional, whereas m_A and f_A are inversely proportional [1, 3]:

$$m_A \simeq 6 \times 10^{-6}\text{eV} \left(\frac{10^{12}\,\text{GeV}}{f_A} \right) . \tag{1}$$

The original axion model developed by Peccei, Quinn, Weinberg and Wilczek (PQWW) introduced a complex scalar field that was known as the "visible" axion [4]. The PQWW model was later experimentally excluded because of the low energy scale $f_{A,weak}$, which produced axions heavier than experimental constraints allowed (discussed in Section 2.3) [1]. Further models have since been constructed, under new constraints; these axions have been dubbed "invisible" as they were originally impossible to detect via experiment. There are two leading models of the invisible axion, the DFSZ and the KSVZ models which are based on the PQWW model but add a $SU(2) \times U(1)$ singlet field – a scalar field carrying a Peccei-Quinn (PQ) charge. These models restrict the mass and coupling parameter space in which one would search for signals. Figure 1 exhibits the vast difference in available parameter space for axions and ALPs, in particular the invisible DFSZ and KSVZ models exist in the relatively small dark red region.

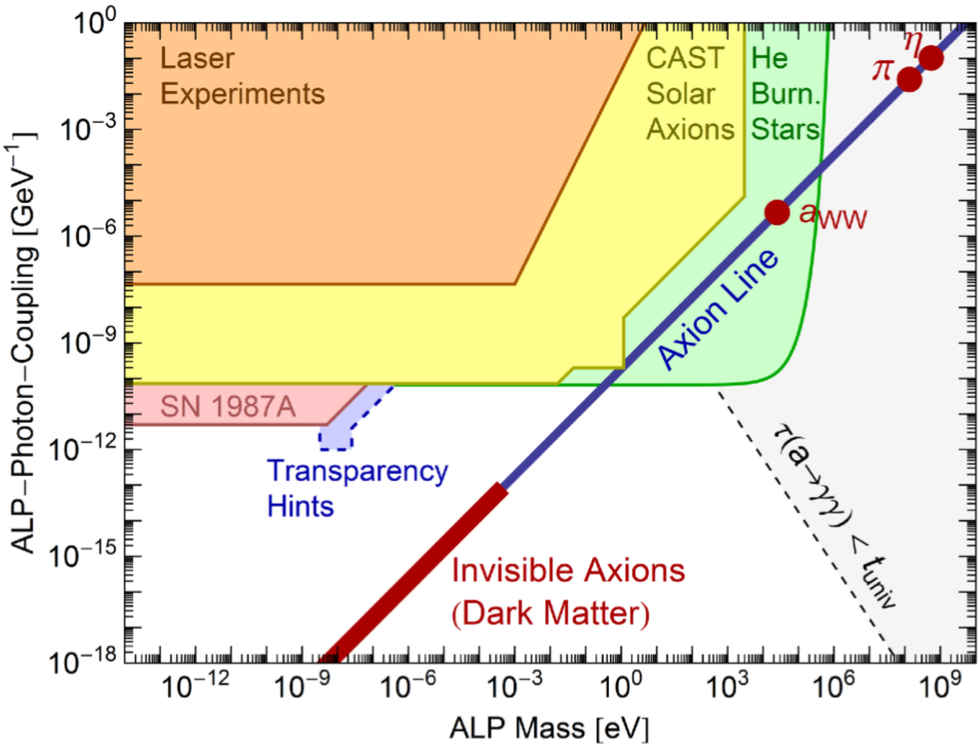

Figure 1: A graph of ALP mass [eV] vs. ALP photon coupling [GeV^{-1}] displaying the parameter space for axions and ALPs with couplings limited by various methods [5]. Within this space is the constrained axionic parameter space (dark blue) and that of the even more constrained invisible KSVZ and DFSZ axions (dark red).

The DFSZ axion arises in a Grand Unified Theory (GUT) – a theory in which the three gauge interactions of the SM become a singular force at a grand unification energy. The DFSZ model allows axions to couple to SM quarks and leptons at the tree-level due to the requirement that they must also carry a PQ charge [6]. In contrast, the KSVZ axion is a hadronic model. This means that axions of this type would only couple to heavy quarks, unlike the DFSZ model. Due to the axion-photon coupling $g_{A\gamma}$, the KSVZ axions can still couple to electrons at a higher level, however the process is extremely weak and therefore the axion-electron coupling g_{Ae} in KSVZ axions is strongly suppressed.

In contrast to the axion, the ALP mass m_A and its coupling to photons $g_{A\gamma}$ are unrelated, and are not directly linked to their PQ-like scale [3]. As a result of this, the ALP parameter space is a larger region than that of the invisible axion, thus there is a much wider range of mass and couplings that the ALP could exhibit.

2.2 Cosmological and astrophysical constraints on axions and ALPs

The axion mass m_A, coupling g_A and decay constant f_A can be constrained by the cosmological evolution of the universe, and through observational evidence obtained from astrophysical events.

Axions and ALPs can have various production mechanisms depending on the properties they exhibit. For axions or ALPs to be viable DM candidates they must have a relatively low mass, a lifetime longer than the universe, and a coupling to matter and radiation that is smaller than the weak interaction coupling strength [2]. If an axion or ALP is a Nambu-Goldstone boson, it could be produced in one of three possible cold DM mechanisms: vacuum realignment, string decay and domain wall decay [7]. Cosmologically, which of these mechanisms dominates depends on the evolution of the universe; whether inflation occurs before or after the PQ phase transition and the QCD transition [8]. Cold DM axions and ALPs are constrained to $f_A \lesssim 10^{12}\,\text{GeV}\,\theta_i^{-2}$, for $m_A \geq 10^{-6}\,\text{eV}\,\theta_i^{-2}$, where the θ_i term accounts for the order of cosmic evolution [3] and is taken to be an arbitrary constant that is < 1. If inflation occurs before the PQ phase transition then $\theta_i \sim 1$; if it occurs after $\theta_i \ll 1$, dark matter could consist of axions entirely and f_A could reach a value of $10^{16}\,\text{GeV}$, which is near the grand unification energy [3]. It is currently estimated that the minimum fraction that axions contribute to DM is 37% [9].

Beyond the cold DM production mechanisms, there are thermal production mechanisms: Primakoff production, bremsstrahlung, the Compton-like effect, axio-recombination and axio-deexcitation (henceforth combined and known as "axio-RD"), and production in the nuclear magnetic transition of ^{57}Fe nuclei [10]. These processes can occur in stellar objects and have couplings to different particles. Primakoff production uses the axion-photon coupling $g_{A\gamma}$; bremsstrahlung, the Compton-like effect and axio-RD exploit the axion-electron coupling g_{Ae}; and the nuclear magnetic transition of ^{57}Fe nuclei employs the axion-nucleon coupling g_{AN}.

Axion couplings and other parameters, such as mass, can be constrained further by limits derived from observation of stellar objects. If, for example, the Sun loses energy via axion emission, then enhanced nuclear burning – and therefore an increase in the solar neutrino flux – is expected, which constrains the axion-photon coupling to $g_{A\gamma} \lesssim 7 \times 10^{-10}\,\text{GeV}^{-1}$ [11, 12]. In addition, the energy loss due to axions or ALPs contributes to reducing the helium burning lifetimes of the horizontal branch stars, which further constrains $g_{A\gamma} \lesssim 0.6 \times 10^{-10}\,\text{GeV}^{-1}$ [13]. Finally, the implication of axions or ALPs acting as cooling mechanisms for stellar objects gives limits from white dwarf star observations on the axion-electron coupling of $g_{Ae} \simeq (0.6 - 1.7) \times 10^{-13}\,\text{GeV}^{-1}$;

from red giants, a mass of $m_A \lesssim 9 \times 10^{-3}$, and coupling $g_{Ae} \lesssim 2.5 \times 10^{-13}\,\mathrm{GeV}^{-1}$; and from neutron stars, a mass of $m_A < 2 \times 10^{-2}\,\mathrm{eV}$ [14, 15, 16].

2.3 Direct detection methods of axions and ALPs

Direct direction is one of many possible methods by which axions and ALPs may be discovered. Direct DM detection experiments focus on the scattering of DM particles from the halo of the Milky Way in a detector on Earth. To distinguish between a DM signal and background radiation or thermal noise, experiments use three possible signals: energy deposition in calorimeters through phonon detection, scintillation light through photon detection, or ionisation through electron detection. The search for axions and ALPs in this project focuses on the direct detection methods that search for solar axion-electron coupling interactions through observation and investigation of scintillation photons.

The main axion interaction that direct detection experiments search for is the axio-electric effect. This effect is analogous to the photoelectric effect, however the incident photon that would be absorbed is replaced by an axion:

$$\mathrm{A} + \mathrm{e}^- + \mathrm{Z} \rightarrow \mathrm{e}^- + \mathrm{Z}. \tag{2}$$

where A is an axion, e^- is an electron and Z is a proton. This interaction is shown in Figure 2.

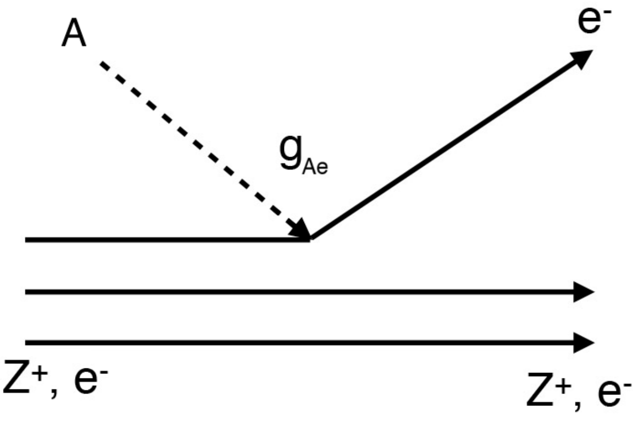

Figure 2: A diagram of the axio-electric effect.

Current direct detection experiments use a range of target materials, from crystals such as germanium (Ge) or sodium iodide (NaI), to liquids such as argon (Ar) or xenon (Xe). Noble liquids have grown to be the dominant material used in direct DM detection experiments due to their useful properties:

- they have high scintillation or ionisation yields which allows detection at much lower energy thresholds,

- their predicted event rate is relatively high,
- they can be cleaned to extremely low levels of radioactivity,
- they are excellent at self-shielding against outside background sources,
- they are transparent to their own scintillation light,
- the sizes of experiments can be of the tonne-scale,
- they generate distinct scintillation pulses for nuclear and electron recoil events, which allows for highly effective discrimination between these events using a method called "pulse shape discrimination" (PSD).

In addition to these properties, on the assumption that the same level of background discrimination against electron and gamma backgrounds can be sustained, the sensitivity of direct DM experiments to the axio-electric effect scales with the mass of the target material.

Current direct detection constraints exist from experiments such as EDELWEISS-II, XENON100, CAST, CoGeNT, and CDMS for various types of axions and ALPs as a function of mass m_A and coupling g_A. For example, the results from the EDELWEISS-II experiment (2013), which made use of the axio-electric effect in Ge, constrains couplings of axions and ALPs; using an exposure of up to 448 kg.d, axion-induced electron recoils were searched for down to 2.5 keV. A limit was set on the axion-electron coupling $g_{Ae} < 2.56 \times 10^{-11}$ (95% CL, shown in Figure 3), and the axion-photon coupling $g_{A\gamma} < 2.13 \times 10^{-9}\,\mathrm{GeV}^{-1}$ (95% CL, shown in Figure 4 as 'Solar-Germanium'). Additionally, $g_{Ae} \times g_{AN}^{eff} < 4.70 \times 10^{-17}$ was constrained, where g_{AN}^{eff} is the effective axion-nucleon coupling for ^{57}Fe. The mass range that was excluded at a 90% CL was $0.91\,\mathrm{eV} < m_A < 8\,\mathrm{keV}$ for DFSZ axions and $5.73\,\mathrm{eV} < m_A < 40\,\mathrm{keV}$ for KSVZ axions [6].

The recent results from the XENON100 experiment (2014), which made use of the axio-electric effect in Xe, presented further constraints on couplings of axions and ALP. A profile likelihood analysis of 7636.4 kg.d exposure showed no evidence of a signal. The best limit to date is $g_{Ae} > 7.7 \times 10^{-12}$ (90% CL) in the solar axion search. In the frame of the DFSZ and KSVZ models, QCD axions heavier than $0.3\,\mathrm{eV\,c^{-2}}$ and $80\,\mathrm{eV\,c^{-2}}$, respectively, were excluded (90%CL). For ALPs, under the assumption that they constitute the whole abundance of dark matter in our galaxy, were excluded for $g_{Ae} < 1 \times 10^{-12}$ (90% CL) in $5 < m_A < 10\,\mathrm{keV\,c^{-2}}$ [17]. This constraint is exhibited in Figure 3.

Competitive limits at higher axion and ALP searches have been set by the axion helioscope technique. The CERN Axion Solar Telescope (CAST) experiment is a helioscope – it searches for axions that have been produced in the Sun using long dipole magnets. An axion that has been produced by the Primakoff process in the Sun can convert to a photon in the dipole magnetic

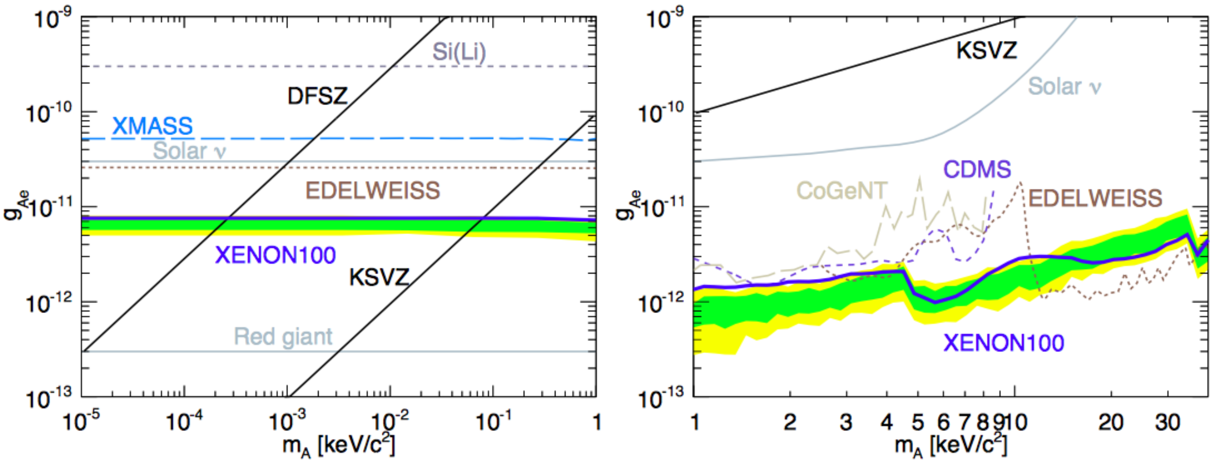

Figure 3: **Left:** Graph of the axion-electron coupling g_{Ae} vs. mass m_a [keV c^{-2}] of the current limits on the solar axion. Limits by XENON100 (blue, 90% CL), with expected sensitivity, based on the background hypothesis, shown by the green/yellow bands ($1\sigma/2\sigma$) [17]. Limits by EDELWEISS-II (dark brown dashed) [6], XMASS (light blue dashed), a Si(Li) detector (grey dashed) [18], indirect astrophysical bounds from solar neutrinos and red giants (grey) [12, 15], and the benchmark DFSZ and KSVZ models (black) are shown. **Right:** Graph of the axion-electron coupling g_{Ae} vs. mass m_a [keV c^{-2}] of the current limits on ALPs. Limits by XENON100 (blue, 90% CL) [17], under the assumption that ALPs constitute all the dark matter in our galaxy. The expected sensitivity is shown by the green/yellow bands ($1\sigma/2\sigma$). Limits by CoGeNT (light brown dashed) [19], CDMS (purple dashed) [20], EDELWEISS-II (dark brown dashed) [6], indirect astrophysical bound from solar neutrinos (grey) and the KSVZ model (black) are shown [12].

field [21]. This photon would be in the X-ray range, would have the same energy as the axion, and would be detected in an X-ray detector at the end of the field. Recent results were published with the bounds $g_{A\gamma\gamma} < 8.8 \times 10^{-11}\,\mathrm{GeV}^{-1}$ at 95% CL for $m_A < 0.02\,\mathrm{eV\,c}^{-2}$ displayed in Figure 4 [22]. Figure 5 shows the CAST limits, and indicates that they managed to cross the KSVZ axion line for masses around 1 eV.

The axion haloscope technique sets the strongest constraints at low masses. The ADMX experiment used the fact that an axion could convert into a resonant, monochromatic microwave signal when passing through a strong magnetic field. It excluded, at a 90% CL, the possibility of KSVZ axions in the mass range $1.9 \times 10^{-6}\,\mathrm{eV} < m_A < 3.53 \times 10^{-6}\,\mathrm{eV}$ [23]. However, they were then revived in this limit due to an uncertainty value that needed to be accounted for. This value was the quark mass ratio $z = m_u/m_d = 0.56$, that could actually hold a value between 0.35 and 0.60 [24]. These results are shown Figure 4.

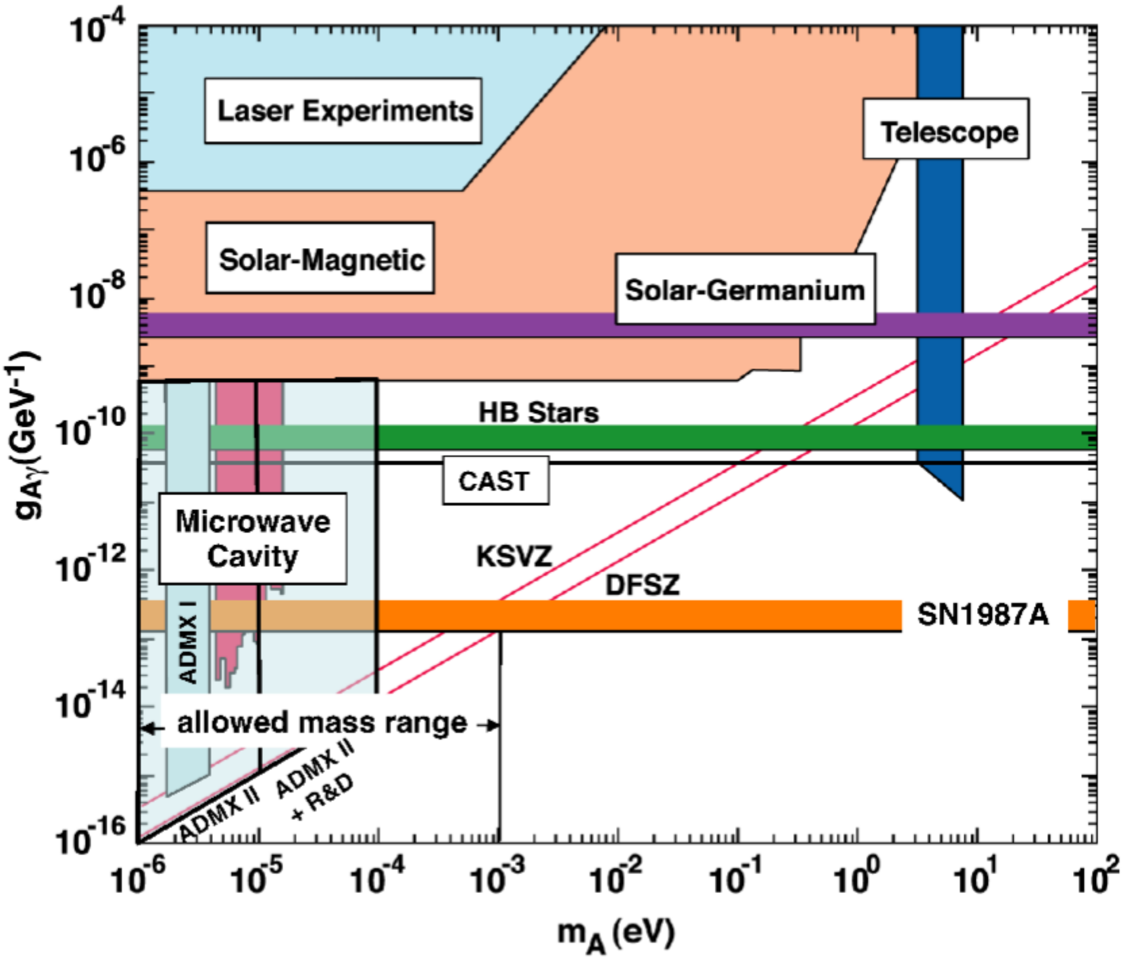

Figure 4: A graph of $g_{A\gamma}$ [GeV^{-1}] vs. m_A [GeV] of the current constrained ALP parameter space [2].

3 The DEAP-3600 detector

The Dark Matter Experiment using Argon Pulse-shape (DEAP-3600) is a direct DM detector with a target material of liquid argon. DEAP-3600 was designed specifically to reach high sensitivities through obtaining extremely low background rates of < 1 background event in 3 years exposure of a 1000 kg nominal fiducial mass. The exposure time in seconds, used throughout this project for scaling, is $\approx 9.46 \times 10^7$ s. This section reviews the DEAP-3600 detector, including the design in Section 3.1 and the method of detection, and distinction, of different types of events in Section 3.2. The prevalent sources of electron-like events in DEAP-3600 are examined in Section 3.3, then Section 3.4 discusses a possible calculation for detector sensitivity.

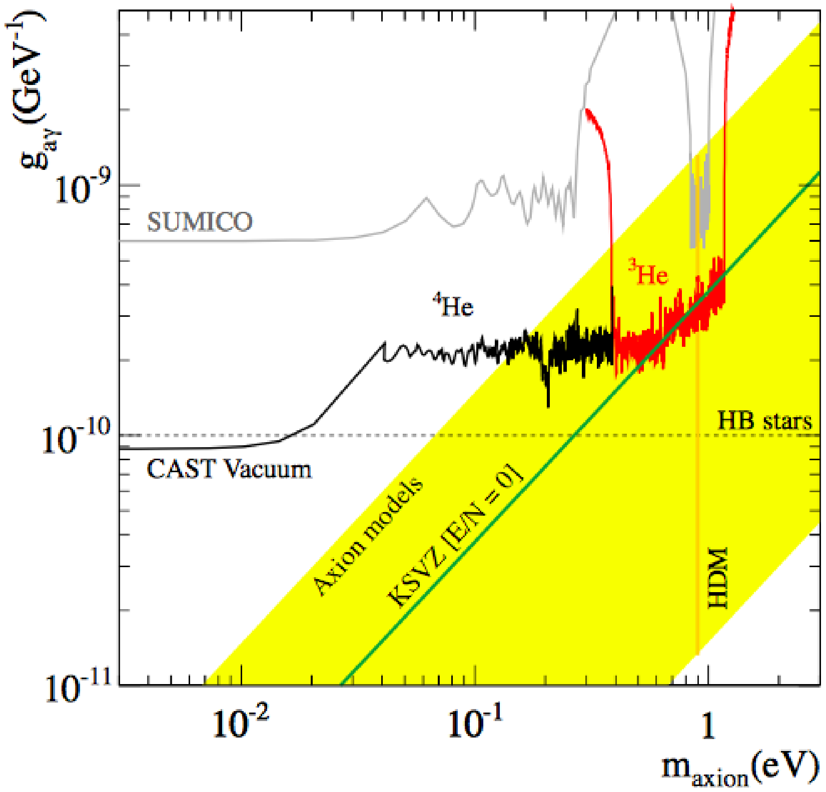

Figure 5: A graph of $g_{A\gamma}$ (Gev^{-1}) vs. m_A (eV) at a 95% CL for CAST Phase I and II results [22]. The theoretical QCD axion models (yellow band) and the KSVZ model with $E/N = 0$ (green) are displayed for comparison. E/N is the model dependent ratio of the electromagnetic anomalies to colour anomalies of the PQ symmetry.

3.1 DEAP-3600 design

The DEAP-3600 detector is situated 2 km underground, and is so named due to the mass of liquid Ar contained within – 3600 kg. Of this, 1000 kg is the nominal fiducial volume, defined by position reconstruction. In addition to the reasons discussed in Section 2.3, liquid Ar was chosen due to its relatively easily accessible temperature of 85 K, its inexpensiveness, and its long light attenuation length. DEAP-3600 is a single-phase detector, which means that it relies on scintillation light alone for particle discrimination. As presented in Figure 6, the Ar is contained within a transparent, cryogenic, spherical acrylic vessel, viewed by 255 8 inch, high quantum efficiency photomultiplier tubes (PMT) through 50 cm lightguides. The lightguides shield the vessel from the much warmer PMTs. The inner vessel is coated with a thin layer of 1,1,4,4-tetraphenyl1-1,3-butadiene (TPB) – a wavelength shifter that converts the argon scintillation light of 128 nm to visible 420 nm blue light, which can then be transmitted through the lightguides to the PMTs efficiently [25]. The inner detector is enclosed in a steel shell, which is immersed in an ultrapure water tank of radius 4 m [26].

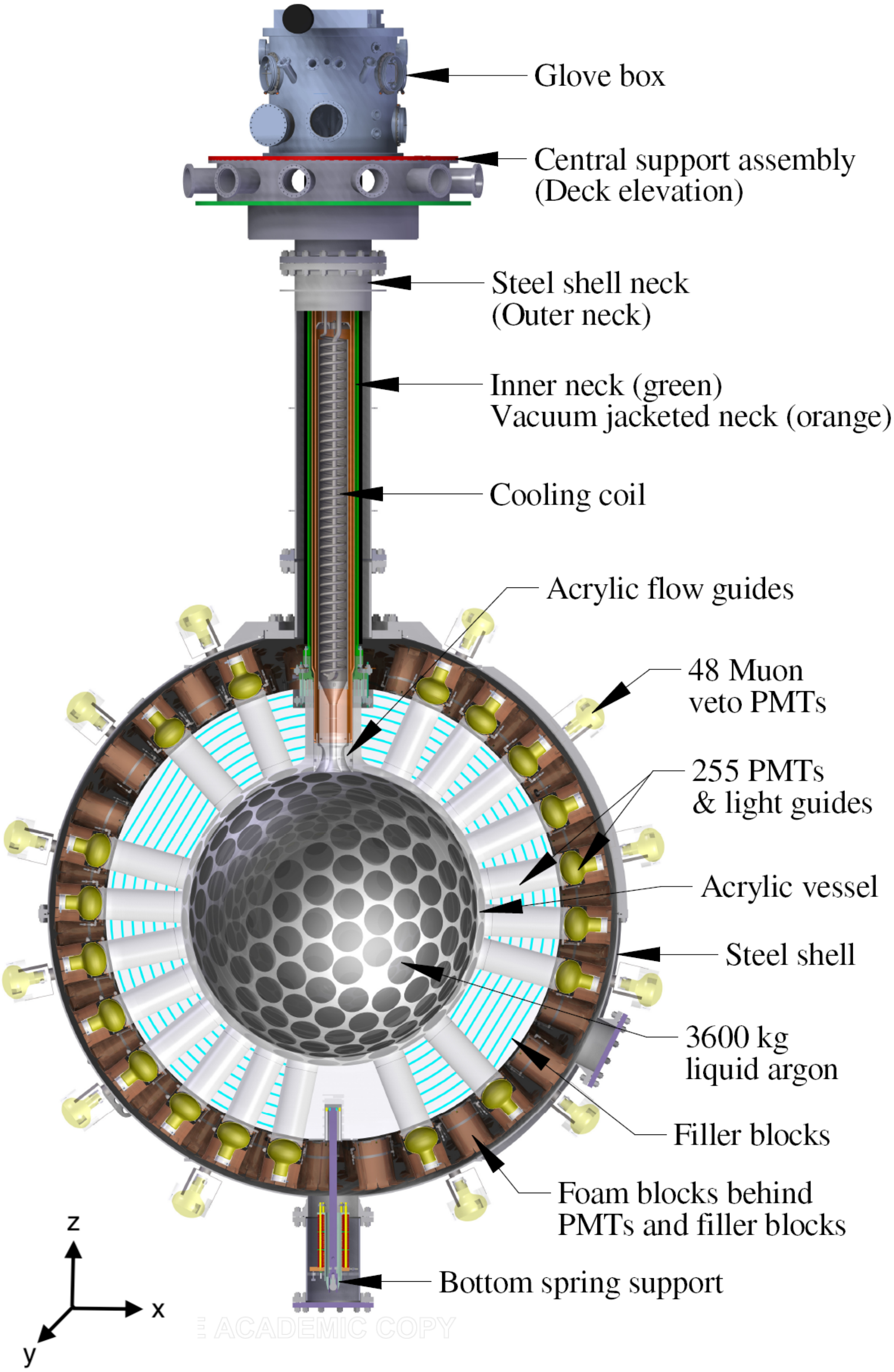

Figure 6: A schematic of the DEAP-3600 detector [27].

3.2 Identification of events

Particle interactions in the liquid Ar target of DEAP-3600 are detected as follows. As radiation passes through the medium it ionises or excites the liquid Ar atoms. Kinetic energy is also imparted to the detector material through elastic collisions with the Ar. The atoms that are excited or ionised form excited diatomic molecular states, or 'excimers'. These excimers exist in two states which have distinct lifetimes: in singlet states, which are short lived (6.7 ns), and in triplet states, which are long lived (1.6 μs)[28, 29]. When these states then decay to their ground state, the scintillation light produced has a peak wavelength of 128 nm. For Ar, a photon of this wavelength is not energetic enough to re-excite another Ar atom and therefore it is transparent to its own scintillation light – a crucial noble liquid property mentioned in Section 2.3. The PMT detects the prompt scintillation signal, which is then used to estimate the energy that has been deposited in the detector and therefore the energy of the recoil. The time dispersion of the scintillation light is characteristic of the type of the particle interaction that has taken place.

The two interactions that are examined in DEAP-3600 are nuclear and electron recoil events. The number of excimers in each state depends on the collision induced transfers. These are different between nuclear and electron recoils due to the particle specific dE/dx. The more energy E dissipated per unit track length, the more singlet states are produced. A recoiling nucleus is slow and heavy, so would deposit all of its energy in a small, localised region in the detector. Nuclear recoil events therefore favour singlet excimers. A recoiling electron, however, is fast and light, and therefore would deposit its energy across a longer track. In this case, due to the increased time available in which to transition to this state, triplet excimers are favoured.

DEAP-3600 has a strong PSD ability, that is, it can distinguish between a nucleon recoil and an electron recoil event through examination of the scintillation time information alone. In DEAP-3600, to make this distinction, one calculates a value called the Prompt Fraction, or "$\mathrm{F}_{\mathrm{prompt}}$". The $\mathrm{F}_{\mathrm{prompt}}$ is the ratio of prompt scintillation light in a pulse (< 100 ns) to the late light in a pulse ($< 15\,\mu$s) and distinguishes electron recoils from nuclear recoils at a level of greater than 1 part in 10^9. $\mathrm{F}_{\mathrm{prompt}}$ is calculated using the $\mathrm{F}_{\mathrm{prompt}}$ processor in the Reactor Analysis Tool (RAT). For a nuclear recoil, the expected value for the $\mathrm{F}_{\mathrm{prompt}}$ is 0.7, whereas for an electron recoil the expected value is 0.3. To determine these values and their spread, a tagged sodium ^{22}Na source and an americium–beryllium neutron source were evaluated in the DEAP-1 detector [30].

3.3 Sources of electron-like events in DEAP-3600

To identify signal events, one must first distinguish between a signal event and a background event. In the search for the axion, the interaction of interest is the electron recoil. Due to the strong PSD of DEAP-3600, one only has to examine the electron recoil events as the nuclear recoil events are identified and removed.

Electron recoils can be caused by electron interactions with photons γ, β particles, and axion signals. Electron-like events could be falsely identified as electron recoil events caused by the axio-electric interaction.

3.3.1 The axion or ALP event

An incoming axion (relativistic or non-relativistic) causes an electron to ionise. The ionised electron forms excimers which decay into photons that are measured by the PMTs. The electron recoils with an energy equal to the axion energy.

As cold DM axions and ALPs are in thermal equilibrium, and the Solar System has a relatively low velocity ($\sim 220\mathrm{km\,s^{-1}}$) through the DM halo of the Milky Way, they are expected to have a small velocity distribution [31]. Due to this, the dispersion of axion and ALP energies is expected to be small. In comparison, solar axions are not in thermal equilibrium, and therefore would have a larger velocity distribution, hence the energy dispersion is expected to have a much more smeared Poisson distribution. When they interact with electrons via the axio-electric effect, the electron recoils are expected to have that same distribution.

3.3.2 The β decay background event from ^{39}Ar

The dominant electron-like event in DEAP-3600 is the β decay of ^{39}Ar. It has a half life of 269.2 years and decays by

$$^{39}\mathrm{Ar} \rightarrow ^{39}\mathrm{K} + \beta^- + \nu\,. \tag{3}$$

^{39}Ar is also produced through neutron capture by ^{39}K. To reduce the rate of β particles from ^{39}Ar decay, and therefore achieve an increased sensitivity for DEAP-3600, natural argon was used as the target material; this has a possibility of reducing the ^{39}Ar level in Ar by a factor of 10^3. In DEAP-3600, the rate of ^{39}Ar is $1\,\mathrm{Bq\,kg^{-1}}$, or $\sim 9 \times 10^4$ decays $\mathrm{kg^{-1}\,day^{-1}}$.

The β particles can produce electron recoil events via ionising Ar atoms. These ionised atoms would create excimers which decay via emitting photons, just as the axio-electric effect does. This is a major issue in the search for axions as the photons emitted have energies that span over the same range expected for axio-electric recoils; they therefore mimic the axio-electric signal. To remove the ^{39}Ar background from the data, the spectrum needs to be measured with very large statistics. Once properly defined, it may be subtracted from the data set to allow the search for axions.

3.3.3 Background events from the uranium and thorium decay chains

The long uranium ^{238}U and thorium ^{232}Th decay chains have many different α, β, and γ decays, and are present in the surrounding rock of the detector. Within this decay chain, and of particular concern to the experiment, is radon ^{222}Rn and ^{220}Rn. Although it decays via α decay, that is, does not resemble the axio-electric effect, it can move through the detector materials, eventually decaying to an isotope via β and/or γ decay. To prevent this contamination of Rn, exposure to air must be limited during the manufacture of the detector and the surface of the detector must be sanded before operation [32]. Potassium ^{40}K is also present in the surrounding rock. As it is a β and γ emitter, these decays can also cause electron recoil events. The β decays mimic axio-electric events in the same way as described for ^{39}Ar β decays in Section 3.3.2. The γ rays can produce Čerenkov radiation from electron-Compton scattering in the acrylic of the detector, which in turn can mimic axio-electric events.The ultrapure water tank shields DEAP from the majority of these particles, however there is still a γ background present in DEAP-3600. The level of radiation is small compared to the ^{39}Ar, at $\lesssim 1\%$ of the Ar background, but it would still be significant in searches for axions.

3.3.4 Effective pile-up of events

There is the possibility of effective pile-up within DEAP-3600. The rate of ^{39}Ar decay is 36kHz ($1\,\mathrm{Bq\,kg^{-1}}$), therefore, because there are so many events, there is a small probability that after the first observed event of ^{39}Ar decay, there is a second event close enough in time that its late scintillation contributes photons to the first event. This second event could be another ^{39}Ar β decay, or a Čerenkov event. This could alter the $\mathrm{F_{prompt}}$ such that an electron recoil event is imitated. This effect would also modify the tail-off, and would be a broad modification at the low energy end of, the ^{39}Ar decay spectrum. It would probably contribute around a 3.5% electron recoil background to the DEAP-3600 background which, although low, is still a significant percentage for searches for axions and ALPs. To veto these events, a cut requiring a minimum of $200\,\mu$s between events can be applied to data.

3.4 The sensitivity of DEAP-3600 to electron-like events

Detector sensitivity depends on the interaction cross section, and the mass, noise, and protection material of the detector. To determine the sensitivity of the detector to a cross section of an interaction, the Poisson method can be used [33]. This method of sensitivity estimation is a conservative approach due to the assumption that there is no knowledge on the background or the event distribution, so each recorded event would be considered as an axio-electric interaction.

The issue with this is that, if any background signals are observed, the sensitivity limit will be overestimated.

To obtain a sensitivity to a 90% CL, the cross sectional value σ as a function of each mass could be determined, such that [33]:

$$1 - \alpha(\sigma) = 1 - e^{-N_{\text{exp}}} \sum_{m=0}^{N} \frac{N_{\text{exp}}^{m}}{m!} = 0.9\,, \tag{4}$$

where α is the CL, σ is the cross sectional value, N is the observed number of events, and N_{exp} is the expected number of events.

4 Detecting solar axions with DEAP-3600

Of particular interest in this project are axions or ALPs that have been produced via the thermal processes in the Sun that were discussed in Section 2.2. The flux of solar axions at the Earth's surface produced in this manner has been accurately predicted by EDELWEISS-II for axion masses between 0 and 14.4 keV, and the expected rate of interaction of these particular particles within DEAP-3600 can be calculated [6]. This rate is calculated in Section 4.1.

As mentioned in Section 2.3, axions can be detected through the axio-electric effect. An axion of energy E incident on the target material would cause an electron recoil of the same energy within the DEAP-3600 detector. Section 4.2 explains the processes used to simulate energy distributions of these electron recoils, and therefore the axions incident on the target material. Section 4.3 then discusses the process of setting a limit on the axion coupling from the results of Sections 4.1 and 4.2.

4.1 Predicting the axion rate at DEAP-3600

The expected interaction rate of axions incident at DEAP-3600 can be calculated using:

$$\text{Rate} = \Phi \times n \times \sigma_{Ae}\,, \tag{5}$$

where Φ is the flux of solar axions at the Earth's surface, σ_{Ae} is the cross section of the interaction, and n is the number of targets within the detector. Here the cross section is defined by the interaction that takes place, which is the axio-electric effect.

4.1.1 Calculating the axio-electric cross section

As the axio-electric effect is analogous the photoelectric effect, the axio-electric cross section can be calculated with the use of the photoelectric cross section. To obtain the photoelectric cross section as a function of photon energy, a fit was applied to the photoelectric absorption spectrum of Ar, which is shown in Figure 7. The fit parameters were determined using CERN's ROOT graph fitting function. Using an equation for a straight line on a log-log graph scale:

$$y = 10^{p_1 \log(x) + p_0} \, , \tag{6}$$

where p_0 and p_1 are the fit parameters of the y-intercept and the gradient, respectively. The photoelectric cross section at energies below 1 keV did not appear in the dataset used, and at lower energies does not follow the logarithmic trend, therefore the logarithmic fits did not apply to these values. For the purposes of this project the values below 1 keV were disregarded with the intention to model lower energies more precisely in the future.

To examine the goodness of fit, the $\chi^2/\mathrm{N_{DoF}}$ was examined. The equation used for the χ^2 was:

$$\chi^2 = \sum_{i=0}^{N} \left(y_i\left(x_i\right) - f\left(x_i; \vec{\theta}\right) \right)^2 \, , \tag{7}$$

where $y_i\left(x_i\right)$ is the data taken from Reference [34], and $f\left(x_i; \vec{\theta}\right)$ is the fit function of the data. Here the x_i are the data points, and $\vec{\theta}$ are the parameters for the fit. The $\mathrm{N_{DoF}} = n - m$, where n is the fit range or number of points, and m is the number of parameters being fitted. Table 1 shows the parameter values of the fits and the values required for $\chi^2/\mathrm{N_{DoF}}$, where $\mathrm{N_{DoF}}$ is the number of degrees of freedom. It can be seen that $\chi^2/\mathrm{N_{DoF}} \gg 1$. For development of the axion detection method, this fit can be used but will not produce reliable axion rates. It should be noted that attempts were made to refit this data with the use of a spline method, and an interpolation method between a few data points, but the methods used produced fits with errors, or even larger $\chi^2/\mathrm{N_{DoF}}$ values.

Table 1: Tables of the parameters for the fit of the photoelectric cross section of Ar. **Left:** displays the fit parameters between $1 \leq \mathrm{E} < 3$ keV. **Right:** displays the fit parameters between $3 \leq \mathrm{E} < 12$ keV.

Parameter	Value
p_0	5.324 ± 0.001
p_1	-2.63 ± 0.01
χ^2	5.7×10^5
$\mathrm{N_{DoF}}$	2
$\chi^2/\mathrm{N_{DoF}}$	2.9×10^5

Parameter	Value
p_0	6.20 ± 0.02
p_1	-2.51 ± 0.04
χ^2	4.46×10^6
$\mathrm{N_{DoF}}$	7
$\chi^2/\mathrm{N_{DoF}}$	6.7×10^5

The discontinuity visible at 3.2 keV in Figure 7 is an "absorption edge" which is due to Ar electron shell energies – the binding energies of electrons for the bound shells of atoms. For photons with energy just above the absorption edge, the photon energy is just sufficient to

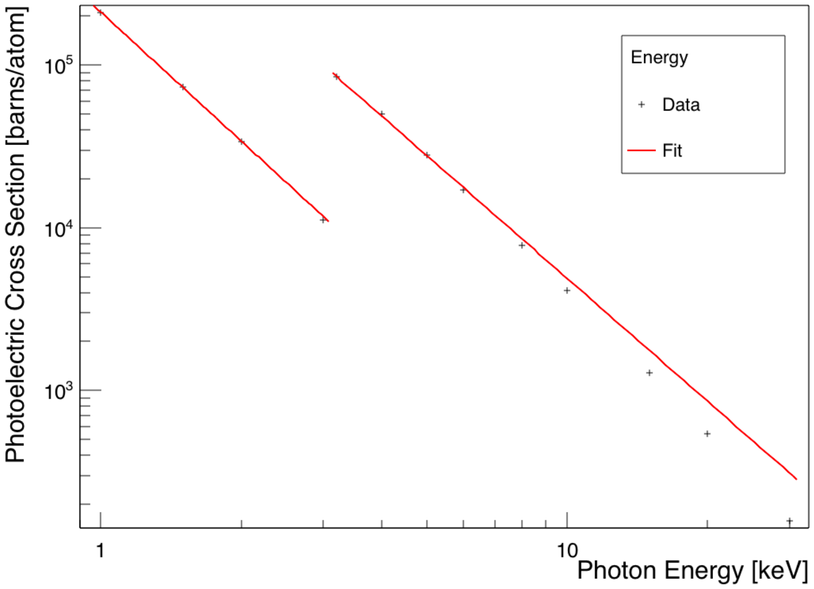

Figure 7: A graph of photoelectric cross section [barns/atom] vs. photon energy [keV] displaying the photoelectric cross section as a function of energy for Ar. Data from [34].

interact with the shell electron. This interaction has a much higher probability than that of photons of energy just below this edge - a photoelectric interaction with an electron in the next shell is impossible, so the probability drops substantially [35].

The axio-electric cross section as a function of axion energy was then estimated using [36, 37]:

$$\sigma_{Ae} = \sigma_{pe}(E_A)\frac{g_{Ae}^2}{\beta_A}\frac{3E_A^2}{16\pi\alpha_{em}m_e^2}\left(\frac{1-\beta_A^{2/3}}{3}\right), \tag{8}$$

where σ_{pe} is the photoelectric cross section for Ar, E_A is the axion energy, α_{em} is the fine structure constant, β_A is the axion velocity divided by the speed of light, m_e is the mass of the electron, and g_{Ae} is the axio-electric coupling. The axio-electric cross section has been represented for several different axion masses in Figure 8. The photoelectric cross section σ_{pe} was calculated using the fit from Figure 7, therefore the 0 keV axion mass is not representative of the true axio-electric cross section at this value. It can be observed that the absorption edge discontinuity is also a property of the axio-electric cross section.

4.1.2 Determining the axion flux at DEAP-3600

The expected (mechanism-dependent) flux of solar axions at the Earth's surface shown in Figure 9 was obtained graphically by digitising the same graph from Reference [6]. This graph was then converted to a histogram, as shown in Figure 10.

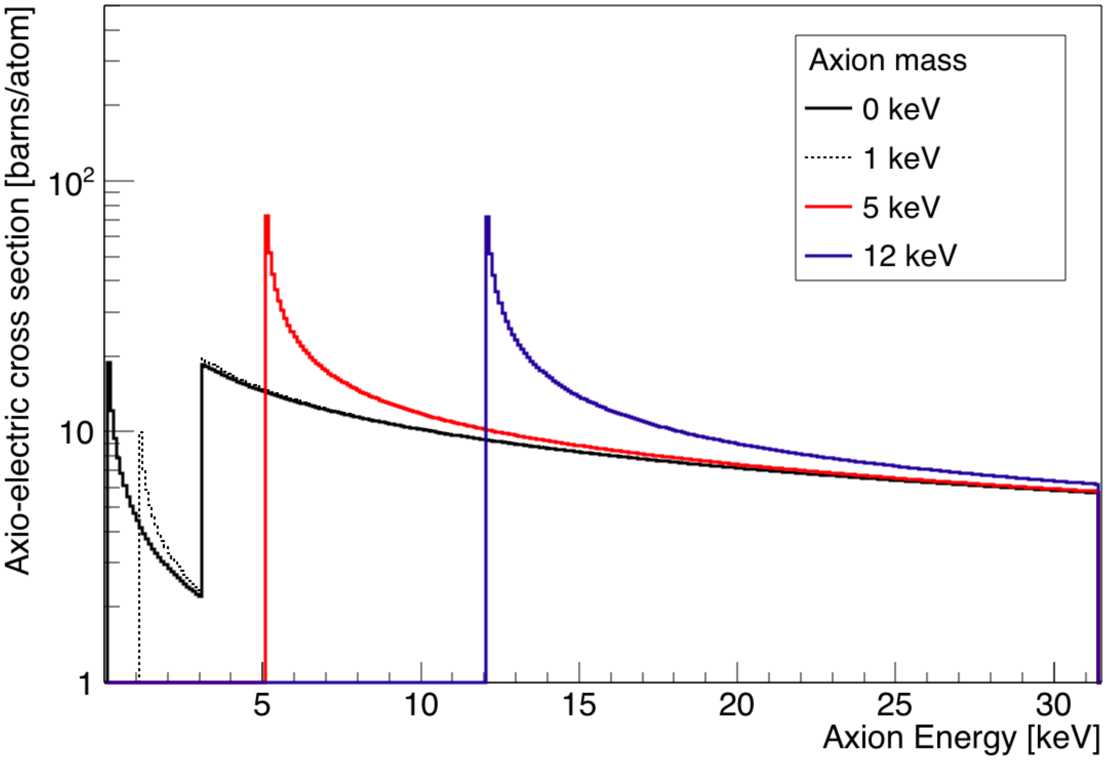

Figure 8: A graph of axio-electric cross section [barns/atom] vs. axion energy [keV] displaying the axio-electric cross section for various axion masses in argon. This graph was constructed assuming the coupling of $g_{Ae} = 1$.

4.1.3 Calculating the number of targets within DEAP-3600

The number of targets n was calculated from the total target mass of Ar available in the detector. As Ar has a mass of $m_{Ar} = 39.94\,\mathrm{u} \simeq 6.6 \times 10^{-26}\,\mathrm{kg}$, there are 5.4×10^{28} atoms of Ar in DEAP-3600. Ar has an atomic number of 18, so there are 18 electrons associated with an Ar atom. Therefore, of the 3600 kg, one has an electron target mass of 0.89 kg, and the number of targets n within DEAP-3600 is $\sim 9.8 \times 10^{29}$.

4.1.4 The resulting rate at DEAP-3600

Using Equation 5, the rate of events expected at DEAP-3600 was calculated as a function of various axion masses and these rates are shown in Figure 11. The coupling has been assumed to equal $g_{Ae} = 1$. By examination of the flux in Figure 10, the highest flux occurs between 3 and 7 keV. When compared to the axio-electric cross section in Figure 8, which has the highest values after the absorption edge, it can be presumed that the highest rate would be expected to occur between 3 and 7 keV. Figure 11 indicates that, of the integer solar axion masses, the 3 keV axion has the greatest rate at the Earth's surface. The 0 keV axion is excluded from analysis at

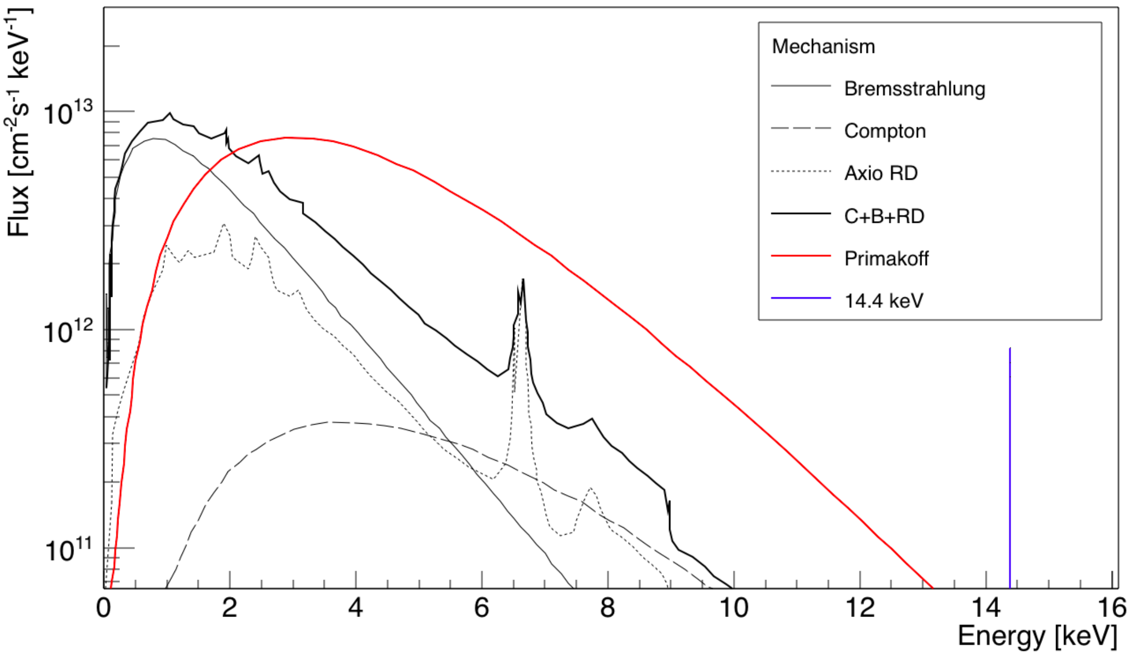

Figure 9: A reproduced graph of flux [cm^{-2}s^{-1}keV^{-1}] vs. energy [keV] displaying the predicted solar axion fluxes of axions at the Earth's surface [6]. Each line represents each production mechanism. 'Axio RD' is the sum of axio-recombination and axio-deexcitation production mechanism fluxes, and 'C+B+RD' is the sum of the Compton, Bremsstrahlung and Axio RD production mechanism fluxes.

this point due to reasons stated in Section 4.1.1.

4.2 Axion signal electron energy distribution

The Monte-Carlo method was used to simulate the axion-induced recoil energy distribution of electrons within the DEAP-3600 detector. Firstly, for each electron recoil event, a 3D momentum vector and 3D position were generated. This electron recoil energy spectrum was then sent for simulation with the RAT external generator.

Each 3D momentum vector was created by generating a total momentum vector $\mathbf{p}_{tot}$ through the use of the equation:

$$\mathbf{p}_{tot} = \sqrt{E^2 - m_A^2}\,, \tag{9}$$

where E is energy of the incident axion and m_A is the mass of the incident axion. The energy distribution of the electron recoil events at DEAP-3600 would be affected by the expected rate of solar axions within the target material. Therefore the rate was taken into account for the energy distribution via use of the acceptance-rejection method. From a randomly generated energy value, uniformly distributed between 0 and 16.1 keV, a second random number was generated for a rate between 0 keV and 1×10^{18} keV^{-1} s^{-1}. If this value was below the maximum rate

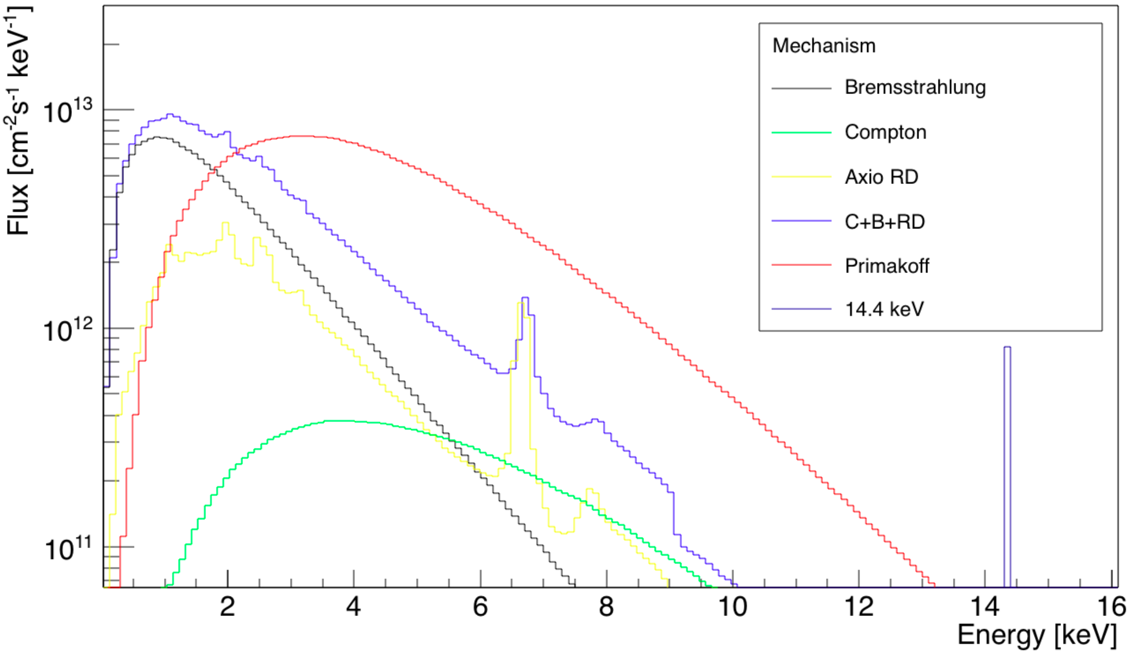

Figure 10: A histogram of flux [cm^{-2}s^{-1}keV^{-1}] vs. energy [keV] displaying Figure 9 in the form of a histogram [6].

at that energy in Figure 11 then it was accepted; if not, it was rejected. The energy range $0 < E < 16.1\,\mathrm{keV}$ was taken to be the upper limit for the mass of solar axions at the Earth's surface due to the maximum limit from Figure 9). The maximum rate of $1 \times 10^{18}\,\mathrm{keV}^{-1}\,\mathrm{s}^{-1}$ was chosen for the inclusion of the highest rate of the 3 keV axion. The mass of the incident axion m_A was determined by the user. The 3D momentum vector was then split into p_x, p_y and p_z components.

The 3D position of each axion event was generated within the detector active volume. This was achieved through the production of random spherical polar coordinates within a radius $r = 850\,\mathrm{mm}$. The spherical acrylic chamber has a radius of $r = 850\,\mathrm{mm}$, with a cut of 550 mm in the z direction due to the liquid Ar level. If the particle was not situated within $z = 550\mathrm{mm}$, it was discarded and the process was repeated. The success of this cut is shown in Figure 12.

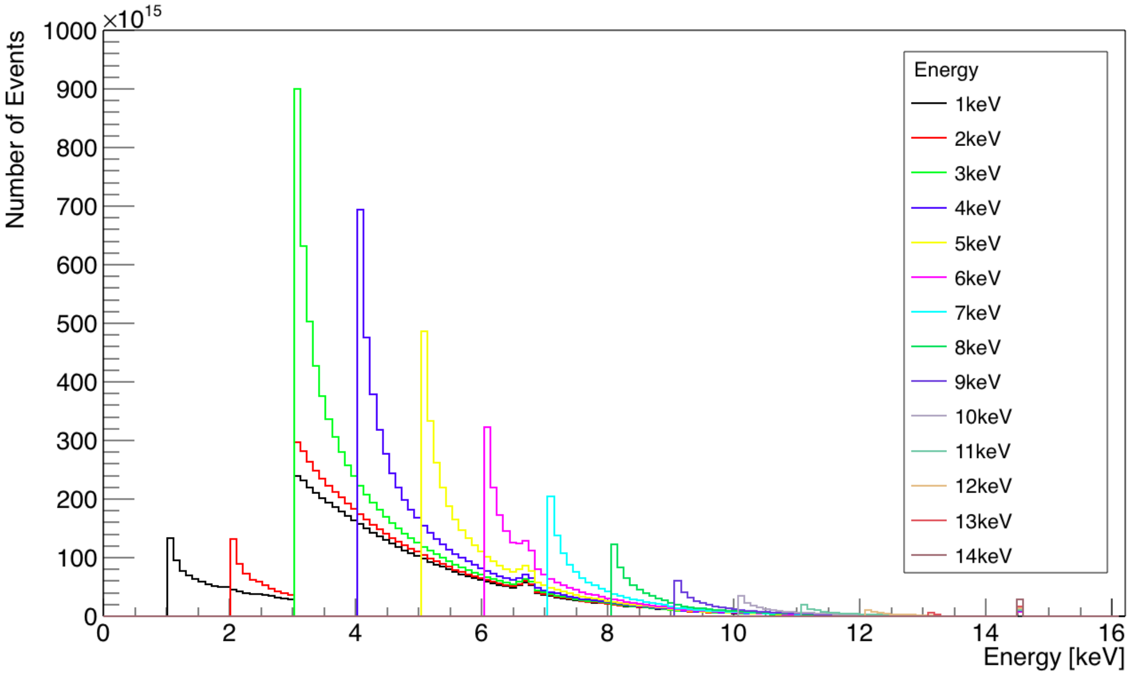

Figure 11: A histogram of rate [$s^{-1}keV^{-1}$] vs. axion energy [keV] displaying the expected rate of axions to be detected at DEAP-3600 as a function of axion mass.

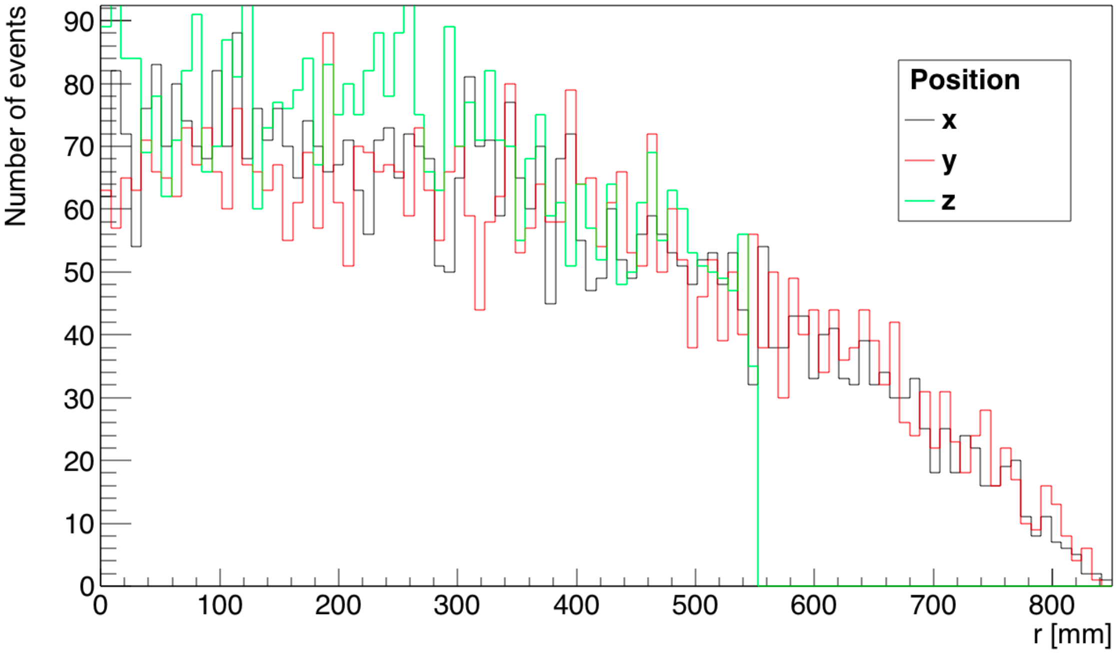

Figure 12: A graph of number of events vs. distance from the centre of the detector [mm], displaying an example of the distribution of 1×10^4 axion events generated for an axion of $m_A = 5\,\text{keV}$.

4.3 The process of setting a limit on the axion coupling

This section uses of the results from Section 4.2 of the axion signal event generator for discussion of the analysis method. To identify the signal of an axion within a set of data, one has to veto the other electron-like events from the data set. To do this one would subtract a well defined ^{39}Ar decay spectrum from a data set that contains only axio-electric interactions and ^{39}Ar decays. In this project, the ^{39}Ar decay spectrum will be approximated to a best fit, and will be calculated in 4.3.3.

To calculate the number of expected events axio-electric events, the equation that will be used is:

$$s + b -^{39} \mathrm{Ar}_{\mathrm{bf}}\,. \tag{10}$$

where s is the signal of the axio-electric event, b is the sum of the background events, and $^{39}\mathrm{Ar}_{\mathrm{bf}}$ is the best fit function of the ^{39}Ar decay spectrum. $s + b$ is the data received from DEAP-3600, which in this project will be simulated as the sum of toy axio-electric interaction events and the $^{39}\mathrm{Ar}_{\mathrm{bf}}$ spectrum with errors.

The statistical residual of the data will then be calculated by plotting the ratio of toy data events divided by best fit function of the ^{39}Ar zero mass hypothesis:

$$\left(\frac{s+b}{^{39}\mathrm{Ar}_{\mathrm{bf}}}\right) - 1\,, \tag{11}$$

where the '-1' centres the distribution around 0. This gives a ratio which shows the fraction of axio-electric events to electron-like background events, so that one can examine the variations on this background.

A statistical test is then examined in Section 4.3.5 for use in setting a limit on the solar axion coupling at a 90% CL as a function of axion mass, given the number of observed events versus the reconstructed electron energy.

4.3.1 Obtaining the toy data of the DEAP-3600 detector

The Reactor Analysis Tool (RAT) of the DEAP-3600 detector was used to make an axion signal event generator. This is a simulation tool that is designed to perform the MC simulation and analysis of liquid scintillator experiments that are surrounded by PMTs. The external generator tool within RAT simulates particles of a determined type and momentum, with the option of definition of a time offset, spatial offset, and/or polarization. In this project, no time offset or polarization was given to the generator. The tool was used to predict the distribution of the rate of electron recoil events due to solar axions of energies 1 keV to 14 keV within DEAP-3600. This distribution would include the effect of all of the detector optics, the PMT and electronics resolution, and event reconstruction.

To obtain the ‘signal’ part of the toy data for the search for the solar axion, the axio-electric events were simulated from the electron positions and momenta previously generated. The times of the events were generated by the Poisson time generator included in RAT. This means that the events are distributed according to Poisson distributed times. 1×10^5 events were generated for an axion of energy 1 keV to 14 keV in steps of 1 keV. This number of events was chosen due to a computational time limit, though to improve statistics it should be noted that the ideal minimum of events is 1×10^6 events in order to have a statistical error of only 0.1% of the contents of each histogram bin.

For an axion mass of 5 keV, the $\mathrm{F}_{\mathrm{prompt}}$ vs. qPE is shown in Figure 13. The qPE is a measure of the energy in photoelectrons calculated from the charge of the scintillation light pulse. The pulse measured in a PMT produces a charge proportional to the charge of a photoelectron, which in turn allows calculation of how many photoelectrons were in that pulse. For comparison, approximately the number of photoelectrons per keV in DEAP-3600 is 8 PE/keV. The original value of the PE/keV light yield is 40 PE/keV, however this value is reduced to 8 PE/keV as not all photoelectrons are measured for reasons including: the efficiencies of the PMTs and their coverage of the detector; the neck of the detector which leaves a gap in the coverage; and the TPB efficiency, which although high, still damps the light yield.

For an electron recoil event, the $\mathrm{F}_{\mathrm{prompt}}$ value is expected to be 0.3. The mean value of the $\mathrm{F}_{\mathrm{prompt}}$ for this graph is 0.4394, due to the spread of events up to a $\mathrm{F}_{\mathrm{prompt}}$ value of 1 at low energies. Though this distribution of events is not centred around $\mathrm{F}_{\mathrm{prompt}} = 0.3$ with a small standard deviation, it is not an unexpected result. The expected statistical fluctuation associated with the number of detected photoelectrons at low energies allows this distribution of events. It is therefore accepted that all of these events are electron recoil events.

For comparison, the $\mathrm{F}_{\mathrm{prompt}}$ versus qPE for highest integer energy in the solar axion search range of 14 keV was plotted and shown in Figure 14. The spread up to $\mathrm{F}_{\mathrm{prompt}} = 1$ still exists but has diminished significantly. In addition, the mean value of $y = 0.3278$ has tended towards the expected $\mathrm{F}_{\mathrm{prompt}} = 0.3$ value. It is expected that the statistical fluctuations at low energies will continue to reduce as axion energies increase.

The simulated energy distributions for 1×10^5 axion interactions obtained from RAT were then examined for axions of energy 1 keV to 14 keV in steps of 1 keV. Figure 15 shows the reconstructed energy distribution of the electron recoils. It has been scaled to the best coupling constraint of the solar axion in this mass range, $g_{Ae} = 7.7 \times 10^{-12}$, discussed in Section 2.3. At energies $\lesssim 38$ qPE, the number of events detected is significantly reduced in comparison to what is expected from the rate histogram in Figure 11. This is due, again, to the low number of PE/keV detected by DEAP-3600 at low energies.

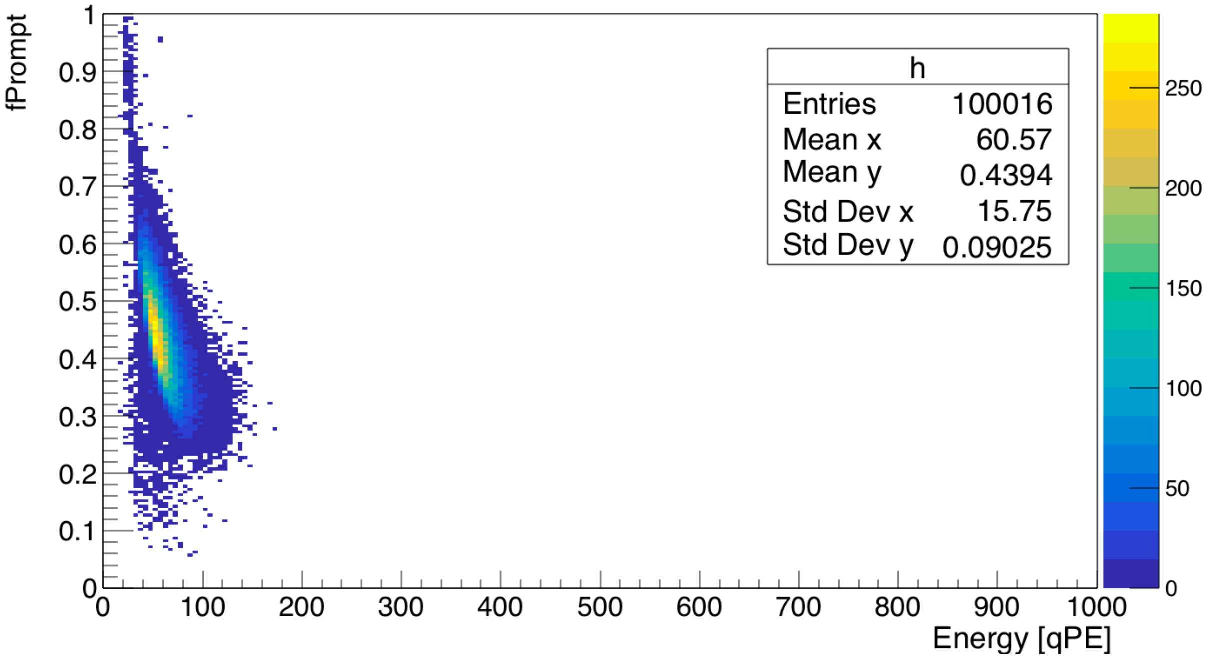

Figure 13: A 2D histogram of F_{prompt} vs. qPE displaying the density of events for axions of 5 keV. One can infer that the events are electron recoil events, due to the mean value of $y = 0.4394$.

To obtain the 'background' part of the toy data, a well defined functional form of ^{39}Ar should be used. An example is shown in Figure 16. However, for analysis in Section 4.3.5, a best fit of the ^{39}Ar decay spectrum (calculated in Section 4.3.3) was used with statistical errors of $\sqrt{N}$.

4.3.2 Applying cuts to the toy data

Within the toy data are possible electron-like events that are not axion-induced. These are from the electron-like sources discussed in Section 3.3. A set of selection general cuts were applied to identify these events and reject them from the toy data. The first of these cuts was the requirement that the maximum fraction of charge that was detected by a PMT (F_{maxPE}) is less than 0.4. The F_{maxPE} takes the charge from an event detected in a PMT and divides it by the total charge detected in the whole detector. This allows the identification, and cut of, events that occur close to the edge of the detector, and background events (such as γ radiation) that could deposit over 90% of their energy in just 1 PMT.

The second cut that was made to the events observed required a minimum of 200 μs between events, to veto the possibility of pile-up of events mentioned in Section 3.3.4.

The third cut was the condition that the events also reside within a radius r of 800 mm from the centre of the detector. This is to make the target mass a fiducial volume of 3000 kg. The final toy data is shown in Figure 17.

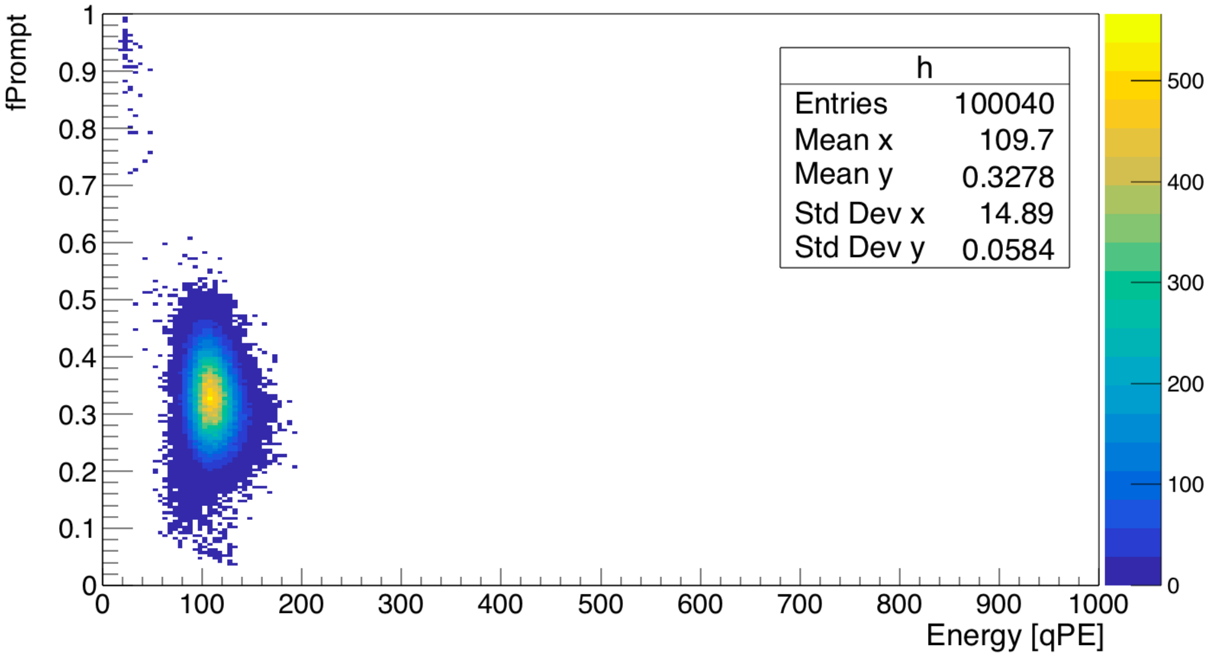

Figure 14: A 2D histogram of F_{prompt} vs. qPE displaying the density of events for axions of 14 keV. From this one can infer that the events are electron recoil events, due to the mean value of $y \simeq 0.3$.

The final cut made to the data was the cut of events existing at a position $z \geq 550\,\mathrm{mm}$. This was to ensure that all of the events were within the liquid level of the DEAP-3600 detector.

4.3.3 Obtaining the best fit of the ^{39}Ar decay spectrum

To obtain the best fit of the ^{39}Ar decay spectrum, a smooth functional form of ^{39}Ar was implemented.

The smooth functional form was calculated using the number of photoelectrons detected versus the kinetic energy of the ^{39}Ar decay spectrum. A Gaussian was then fitted to each bin of the ^{39}Ar decay spectrum histogram, so that the mean (μ) and standard deviation (σ) were calculated. Here the μ is the mean PE, and σ is PE. From the plot of σ versus energy (with error $\sqrt{E}$) and μ versus PE, the smooth functional form of ^{39}Ar was reconstructed through the use of interpolation. To get the energy in PE as a function of energy PE(E), the energy values were summed at the chosen value of PE using:

$$\mathrm{PE(E)} = \int g(\mathrm{E}) \otimes f(\mathrm{PE,\, E}) d\mathrm{E}\,, \tag{12}$$

where $g(\mathrm{E})$ is the spectrum of ^{39}Ar normalised to 1 event, and $f(\mathrm{PE,\, E})d\mathrm{E}$ is the functional form of ^{39}Ar. The result of this calculation, and best fit of ^{39}Ar, is shown in Figure 18. The colour dispersion is due to normalisation of the spectrum at each energy scale to a total probability of

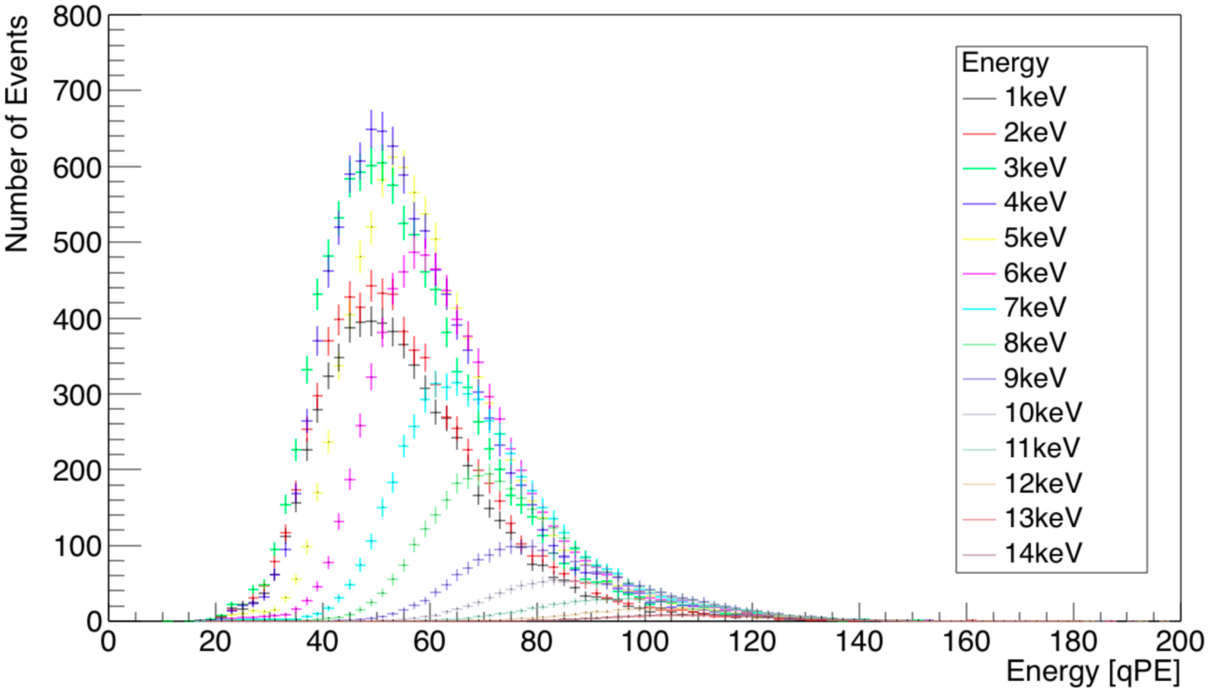

Figure 15: A histogram of the number of axion events versus the qPE of the electron recoil expected at DEAP-3600 assuming a coupling of $g_{Ae} = 7.7 \times 10^{-12}$.

1.

For the purposes of this project the energy scale [PE/keV] was assumed to equal 1, therefore the projection of x at this point of the energy scale of Figure 18 gives the best fit of ^{39}Ar. If in future calculations a change in the energy scale were required, analyses can simply alter the best fit of the ^{39}Ar decay spectrum.

The unscaled best fit of the ^{39}Ar decay spectrum was then scaled to the expected rate of ^{39}Ar decays within DEAP-3600, and the final analytical model of the ^{39}Ar decay spectrum is shown in Figure 19. As the histogram is normalised to 1 event, it has been scaled by the exposure time (defined in Section 3) and the rate of decay. As the expected rate of ^{39}Ar decay is the equivalent of $1\,\mathrm{kHz\,kg^{-1}}$, and the target mass after the z and r cuts is $\sim 2800\,\mathrm{kg}$, the total number of events of ^{39}Ar decay expected over 3 years is $\sim 2.65 \times 10^{14}$. It should be noted that, though purely analytical, this model could carry systematic errors from the fit, however as the true energy resolution is not known this was not taken into account.

The best fit of the ^{39}Ar decay spectrum is shown in Figure 20 together with the reconstructed energy distribution from Section 4.3.1.

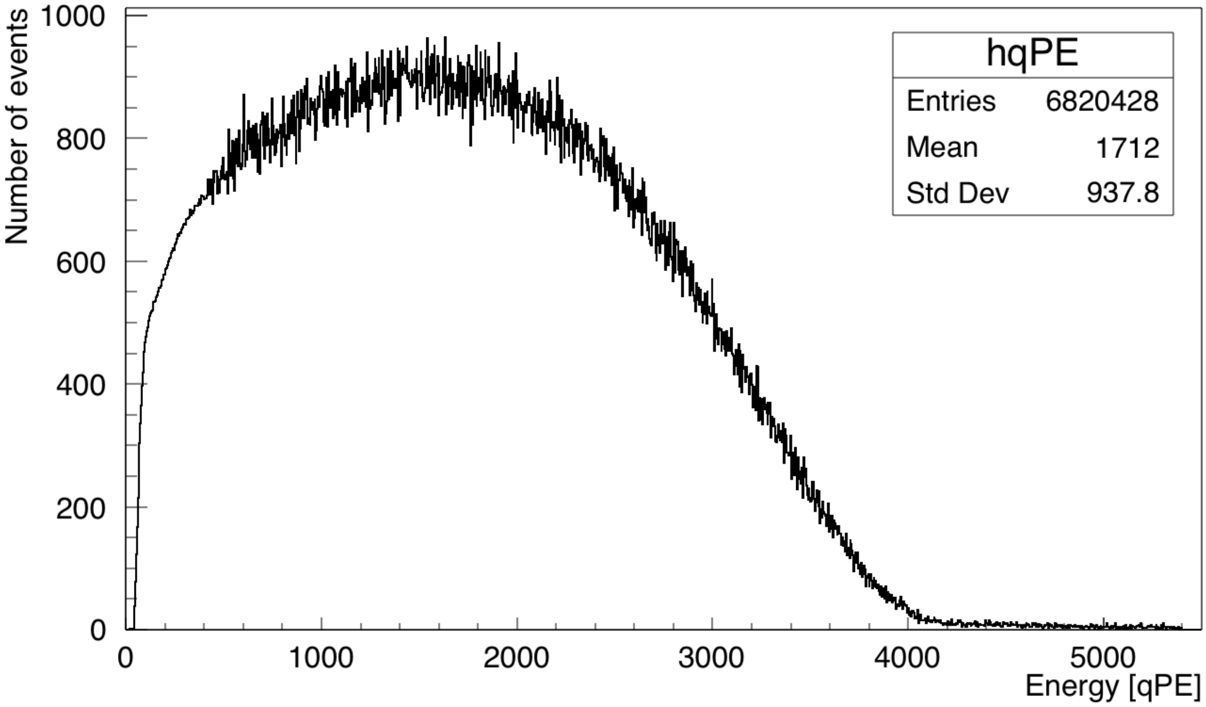

Figure 16: A histogram of number of events vs. energy [qPE] displaying the ^{39}Ar decay spectrum for 9 tonne-years.

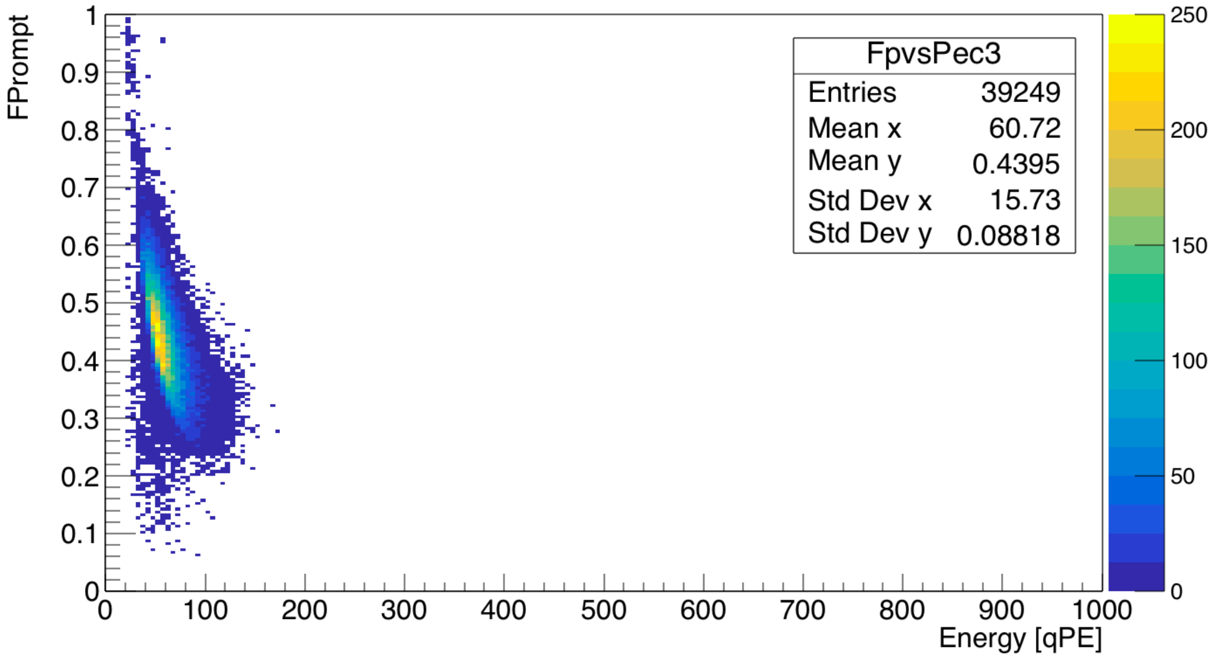

Figure 17: A 2D histogram of F_{prompt} vs. qPE displaying the density of events after the removal of events with $F_{\mathrm{maxPE}} < 0.4$, $z \geq 550\,\mathrm{mm}$ and $r > 800\,\mathrm{mm}$.

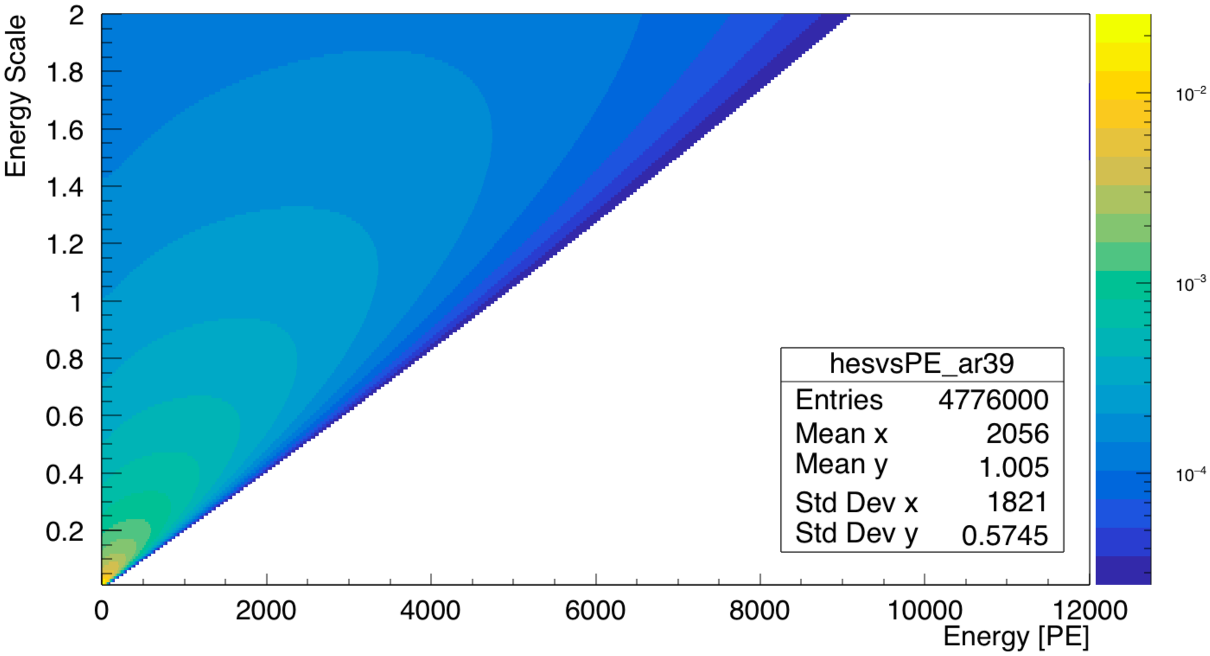

Figure 18: A 2D histogram of energy scale [PE/keV] vs. energy [PE], displaying the best fit form of ^{39}Ar at different energy scales. The z axis, which can be interpreted as dN/dE or probability of decay, is logarithmic.

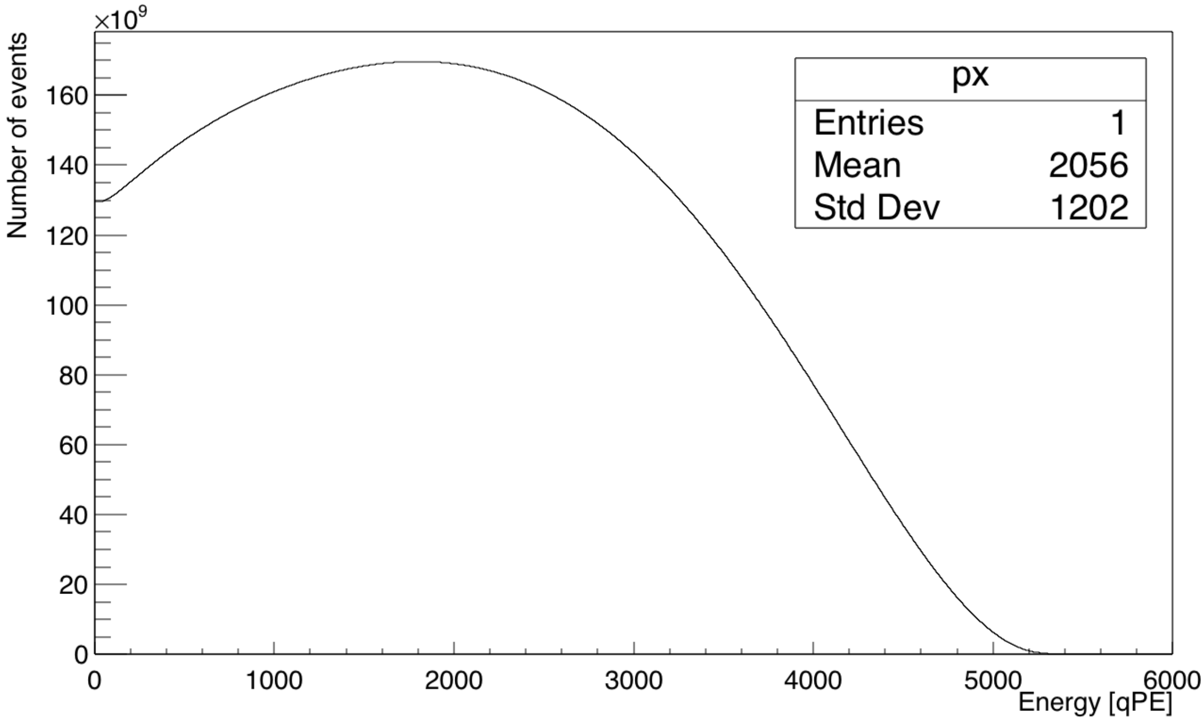

Figure 19: A histogram of number of events vs. PE, displaying the best fit form of ^{39}Ar. It was obtained from taking the x projection of Figure 18 at the energy scale of 1. It has been scaled to 9 tonne-years.

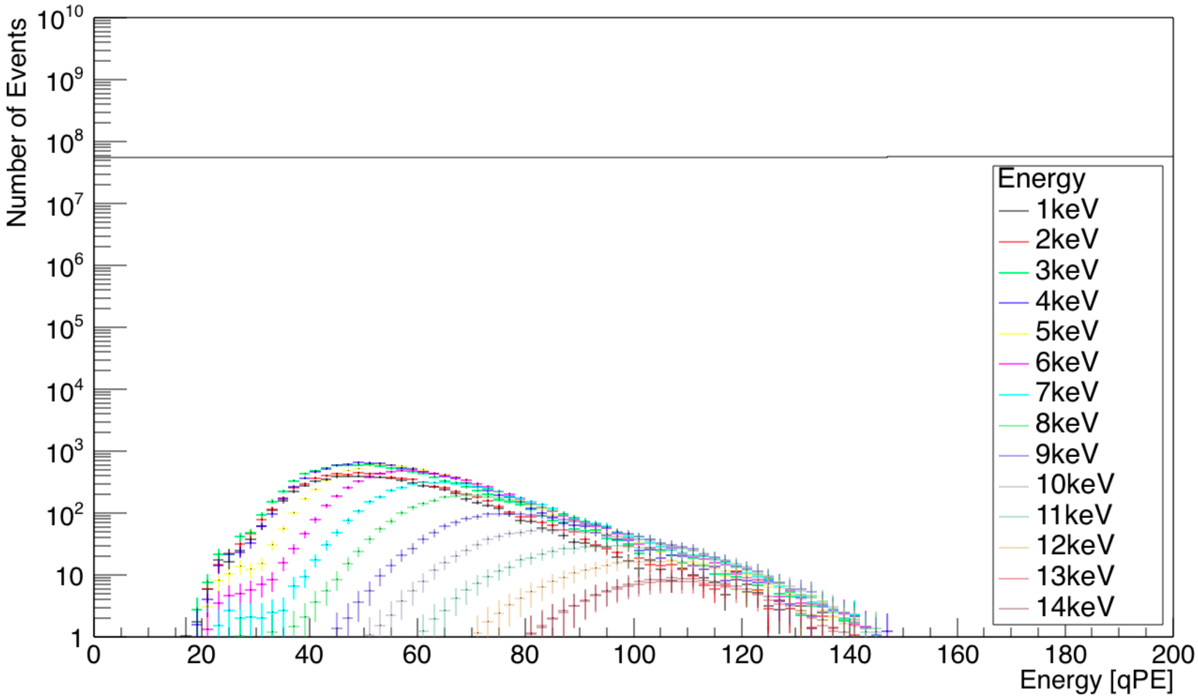

Figure 20: A histogram of number of events vs. energy [qPE] displaying, on a logarithmic scale for comparison, the best fit of the ^{39}Ar decay spectrum (black line) and the ^{39}Ar decay spectrum for 9 tonne-years (coloured error bars).

4.3.4 The search for axions within toy data

The toy data was estimated for the expected electron recoil spectrum observed at DEAP-3600 for an incident axion of energy 5 keV. The data was modelled as the sum of the axio-electric recoil events and the best fit of the ^{39}Ar decay spectrum with errors calculated as $\sqrt{N}$. Through the use of this data and the purely analytical best fit of the ^{39}Ar decay spectrum, Equation 10 was utilized to obtain Figure 21. The errors within this figure were propagated from the errors of the best fit of the ^{39}Ar decay spectrum, and the errors from the electron recoil spectrum.

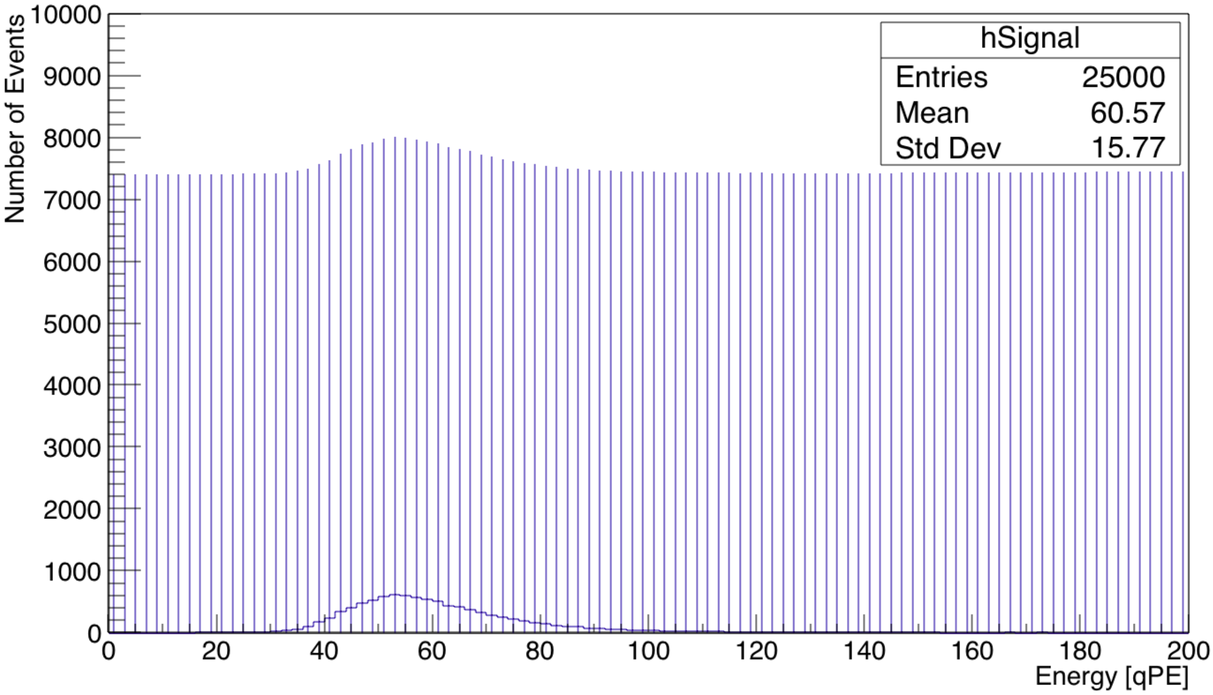

Figure 21: A histogram of number of events versus energy [qPE] showing the number of axio-electric events expected in DEAP-3600.

Equation 11 was then used with the same variables to obtain Figure 22. This is the statistical residual of the data, which exhibits the difference between the observed data and the estimated data, with errors. The observed data in this analysis was the sum of the best fit of the ^{39}Ar decay spectrum and the electron recoil energy distribution, but in future analysis would be actual data from the experiment. The estimated data was the analytical best fit of the ^{39}Ar decay spectrum, presumed to be an ideal model, and therefore have no errors. For future development of these plots, a well defined ^{39}Ar decay spectrum is needed, however the Feldman-Cousins toy Monte Carlo method could be implemented to produce this spectrum with a 90% CL.

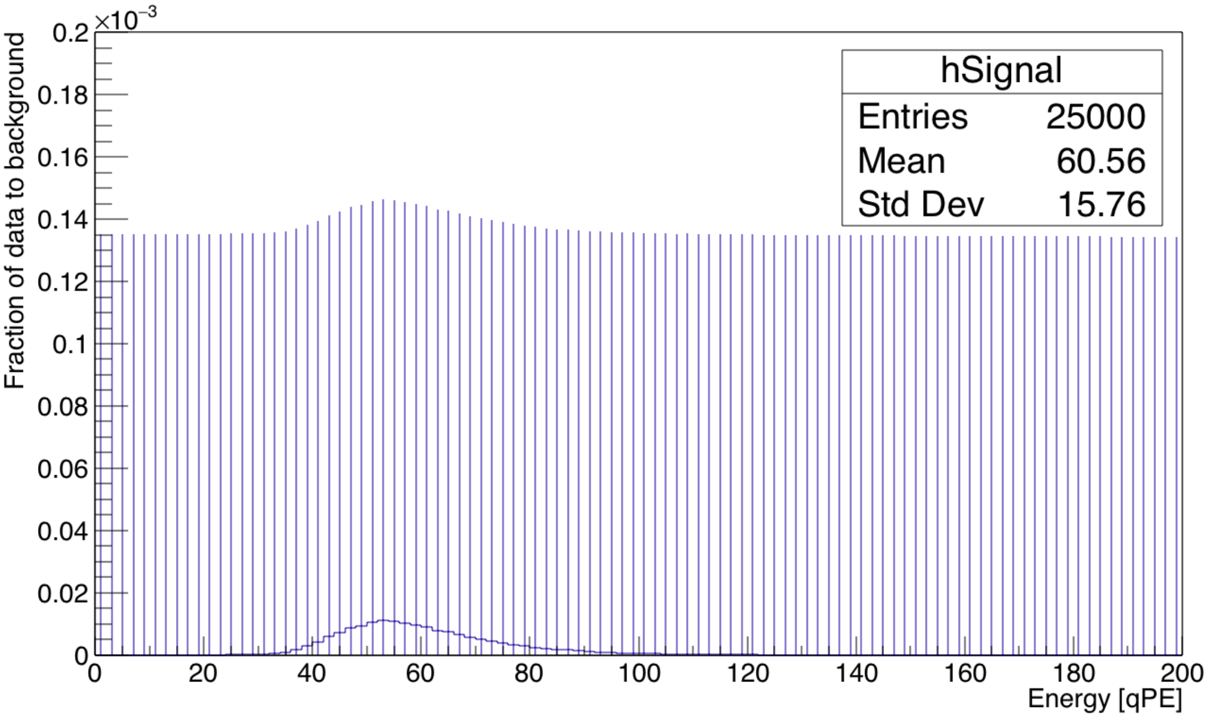

Figure 22: A histogram of the ratio of data events to background events versus electron recoil energy [qPE] showing the ratio of axio-electric events to ^{39}Ar background events expected in DEAP-3600.

4.3.5 The Feldman-Cousins Toy Monte Carlo Method

The best method to determine a confidence region is the likelihood ratio ordering principle, however it requires thousands of toy Monte Carlo (MC) datasets. Feldman and Cousins developed a method to perform these toy Monte Carlo computations [38]. The confidence intervals $[\mu_1, \mu_2]$ of a CL α are computed via construction of a confidence belt that consists of the conjunction of the intervals $[x_1(\mu), x_2(\mu_2)]$. The conjunction of the intervals means that for each μ, one finds an integral such that [39]:

$$\int_{x_1}^{x_2} P(x|\mu)dx = \alpha\,, \tag{13}$$

where $P(x|\mu)$ is the probability density function. In order to solve x_1 and x_2 uniquely, one needs to specify an ordering principle that determines in which order the dx shall be included into the interval. F-C include the dx in order of decreasing likelihood ratio:

$$R(x,\mu) = \frac{P(x|\mu)}{P(x|\mu_{\text{best}})}\,, \tag{14}$$

where μ_{best} is the value of μ that maximises the likelihood $P(x|\mu)$ and is also within the allowed region. It is convenient to express the likelihood ratio as the log-likelihood ratio:

$$-2\ln R = \chi^2 - \chi^2_{\text{best}} = \chi^2(x,\mu) - \chi^2(x,\mu_{\text{best}}). \tag{15}$$

Using the likelihood ratio ordering means that for a given μ, the interval $[x_1, x_2]$ is such that

$$R(x_1) = R(x_2) \tag{16}$$

and the probability density integrals hold. It should be noted that they do not hold as well for discrete probability densities. Feldman and Cousins use toy MC experiments to solve these two equations (Equations 13 and 16).

The toy MC experiments are datasets from the assumed probability density function. In this project, the assumed probability density function is the best fit of the ^{39}Ar decay spectrum. The algorithm computes the interval $[x_1, x_2]$ for each value of μ. Here μ is the true parameter, equal to the mean of the ^{39}Ar decay distribution of events. The combination of all of these intervals gives the confidence belt.

At the considered value of μ, μ_0, one would generate a toy experiment by drawing a value of x_{toy} from the best fit of the ^{39}Ar decay spectrum. The $\Delta\chi^2_{\text{toy}}$ for the toy experiment would be calculated using:

$$\Delta\chi^2_{\text{toy}} = \chi^2(x_{\text{toy}}, \mu_0) - \chi^2_{\text{best}}(x_{\text{toy}}, \mu_{\text{best}})\,. \tag{17}$$

One must then determine the interval $[x_1, x_2]$ by finding a value for $\Delta\chi^2_c$, such that the confidence level α of the toy experiments have a $\Delta\chi^2_{\text{toy}} < \Delta\chi^2_c$. The interval is given by all of the values of x that satisfy this constraint.

5 Conclusion

This project developed a method to search for axions and ALPs interacting in the DEAP-3600 liquid Ar detector. Contrary to WIMP searches, electron recoils were examined as a potential axion or ALP signal. Axions and ALPs can interact with matter via the axio-electric effect, therefore their expected rate of interaction within DEAP-3600 could be predicted using the axio-electric cross section, the number of targets within DEAP-3600, and the flux of axions expected at the Earth's surface. The result of this calculation is shown in Figure 11 with an assumed coupling of $g_{Ae} = 1$.

To examine the success of the method developed, the axion and ALP search was reduced to the search for solar axions of masses $1 \leq m_A \leq 14\,\text{keV}$. This limited search was due to the range of the flux expected of solar axions at the EDELWEISS detector [6], and the fit of the axio-electric effect in Ar.

A Monte Carlo simulation of electron recoils caused by the axio-electric effect in this energy range was created. The recoil electrons were generated at an energy higher than the mass of the incident axion within the DEAP-3600 detector, and altered by the expected rate distribution. These events were simulated through the RAT external generator.

The electron recoil spectrum that was expected from the axio-electric effect for axions between of mass $1 \leq m_A \leq 14\,\mathrm{keV}$ was predicted, and is shown in Figure 15. This was then evaluated with a model of the DEAP-3600 signal to achieve the number of axio-electric events versus the electron recoil energy. Figure 21 shows the result of this for a 5 keV axion. The ratio of axio-electric events to background events was then determined to produce Figure 22.

To augment this project, the fit of the photoelectric cross section would be improved. The issue with the fitting methods, discussed in Section 4.1.1, would have affected each calculation within this project that implemented the axio-electric cross section. This implies that the expected rate at DEAP-3600 calculated and shown in Figures 11 and 21 have large systematic errors that have not been taken into account. For the development of the axion and ALP search method, this fit was adequate, but for reliable predictions of the number of axions interacting within DEAP-3600 this fit must be revised.

Due to time-out issues with the local computer farm, it was not possible to run simulations for events over 1×10^5 events. For further improvement of the statistical errors, and therefore the events simulated, it would have been ideal to simulate at least 1×10^6 events to obtain reduce the error to 0.01% of the number of events detected. In further development of this project, this aim would be achieved.

Future development of this project would be to perform the statistical test described in Section 4.3.5. The toy MC experiments created through drawing from the best fit of the ^{39}Ar decay spectrum would be used to set a limit on the axion coupling at 90% CL as a function of axion mass, given the number of toy observed events versus reconstructed electron energy.

This project would then be extended to search for higher energy axions such as cold DM axions and ALPs via the prediction of the rate of axio-electric interactions within DEAP-3600 for energies $> 14\,\mathrm{keV}$.

Beyond this project is the improvement of the axion rate of interaction within the detector. The plan for the next generation of the liquid argon detector is already in progress; DEAP-50T is an expansion of DEAP-3600, from $3.6 \times 10^3\,\mathrm{kg}$ to $5 \times 10^4\,\mathrm{kg}$. Due to the scalability of noble liquid experiments a target sensitivity of $10^{-48}\,\mathrm{cm}^2$ could be reached. This would be a further factor of 100 increase in sensitivity and, depending on the observations of DEAP-3600, could search further for DM particles, or investigate the properties of a newly discovered DM particle.

References

[1] H.Y. Cheng. The Strong CP Problem Revisited. *Physics Report* **158** (1988) 1; DOI: `10.1016/0370-1573(88)90135-4`.

[2] A. Kusenko, L. J. Rosenburg *Snowmass-2013 Cosmic Frontier 3 (CF3) Working Group Summary: Non-WIMP dark matter.* (2013); ePrint arXiv:`1310.8642`.

[3] J.L. Feng. Dark Matter Candidates from Particle Physics and Methods of Detection. *The Annual Review of Astronomy and Astrophysics* **48** 495 (2010) pp. 46-48; DOI: `10.1146/annurev-astro-082708-101659`.

[4] S. Weinberg. A New Light Boson? *Physics Review Letters* **40** 223 (1978); DOI: `10.1103/PhysRevLett.40.223`.

[5] G. Raffelt. Warsaw Workshop on Non-Standard Dark Matter. (2016) Available Online: `http://indico.fuw.edu.pl/getFile.py/access?contribId=24&sessionId=9&resId=1&materialId=slides&confId=45`. Accessed: 4 Nov 2016.

[6] The EDELWEISS Collaboration: E. Armengaud *et al.* Axion searches with the EDELWEISS-II experiment. *Journal of Cosmology and Astroparticle Physics* **1311** (2013); ePrint `arXiv:1307.1488v1`.

[7] D. J. E Marsh. Axion Cosmology. *Physics Reports* **643** (2016) pp. 1–79; DOI: `10.1016/j.physrep.2016.06.005`.

[8] P. Sikivie. Axion Cosmology *Lecture Notes in Physics* **741**, 19 (2008); ePrint arXiv:`astro-ph/0610440`.

[9] P. Sikivie. Axion Dark Matter Detection using Atomic Transitions. *Physics Review Letters* **113** (2014) 20, 201301; DOI: `10.1103/PhysRevLett.113.201301`

[10] J. Redondo. Solar axion flux from the axion-electron coupling. (2013); ePrint arXiv:`1310.0823v1`.

[11] H. Schlattl, A. Weiss, G. Raffelt. Helioseismological constraint on solar axion emission. *Astroparticle Physics* **10** (1999) pp. 353–359; DOI: `10.1016/S0927-6505(98)00063-2`.

[12] P. Gondolo, G. Raffelt. Solar neutrino limit on axions and keV-mass bosons. *Physics Review***D79** (2009) 107301; DOI: `10.1103/PhysRevD.79.107301`.

[13] G. G. Raffelt. Particle physics from stars. *Annual Review of Nuclear and Particle Science* **49** (1999) 163–216; DOI: `10.1146/annurev.nucl.49.1.163`.

[14] G.G. Raffelt. Axion constraints from white dwarf cooling times. Physics Letters B **166** 4 (1986) pp. 402-406; DOI: `10.1016/0370-2693(86)91588-1`.

[15] G. Raffelt, A. Weiss. Red giant bound on the axion - electron coupling revisited. *Physics Review* D **51** (1995) pp. 1495-1498; DOI: `10.1103/PhysRevD.51.1495`.

[16] D.B. Kaplan. Opening the Axion Window. *Nuclear Physics* B **260** (1985) 215-226; DOI: `10.1016/0550-3213(85)90319-0`.

[17] The XENON100 Collaboration (E. Aprile et al.) First Axion Results XENON100 Experiment. *Physics Review* D **90** (2014); ePrint `arXiv:1404.1455v2`.

[18] A. Derbin *et al.* Constraints on the axion-electron coupling constant for solar axions appearing owing to bremsstrahlung and the Compton process. *Journal of Experimental and Theoretical Physics Letters* **95** 339 (2012).

[19] CoGeNT Collaboration (C. E. Aalseth *et al.*) Experimental constraints on a dark matter origin for the DAMA annual modulation effect. *Physics Review Letters* **101**, 251301 (2008).

[20] CDMS Collaboration (Z. Ahmed *et al.*), *Physics Review Letters* **103**, 141802 (2009).

[21] CAST Collaboration (S. Andriamonje *et al.*) Search for 14.4-keV solar axions emitted in the M1-transition of Fe-57 nuclei with CAST. *Journal of Cosmology and Astroparticle Physics* **0912** (2009) 002; ePrint arXiv:`0906.4488`.

[22] CAST Collaboration (J. Ruz *et al.*) Recent Constraints on Axion-photon and Axion-electron Coupling with the CAST Experiment. *Physics Procedia* **61** (2015) pp. 153-156; DOI: `10.1016/j.phpro.2014.12.025`.

[23] ADMX Collaboration (S. Asztalos *et al.* A SQUID-based microwave cavity search for dark-matter axions. *Physics Review Letter* **104** (2010) 041301; DOI: `10.1103/PhysRevLett.104.041301`.

[24] M. R. Buckley, H. Murayama. Quark mass uncertainties revive Kim-Shifman-Vainshtein-Zakharov axion dark matter. *Journal of Cosmology and Astroparticle Physics* **0707** (2007) 012; DOI: `10.1088/1475-7516/2007/07/012`.

[25] DEAP Collaboration (P. A. Amaudruz *et al.*) DEAP-3600 Dark Matter Search. *Nuclear Particle Physics Proceedings* 273-275 340-346 (2016). DOI: `10.1016/j.nuclphysbps.2015.09.048`.

[26] M.G. Boulay, A. Hime. Technique for Direct Detection of Weakly Interacting Massive Particles Using Scintillation Time Discrimination in Liquid Argon. *Astroparticle Physics* **25** 179-182 (2006); DOI: `10.1016/j.astropartphys.2005.12.009`.

[27] The DEAP Dark Matter Experiment *DEAP-3600 Schematic.* [Online] Available from: `http://deap3600.ca/wp-content/uploads/2015/04/DEAP-3600-detector.png` [Accessed 10th June 2015].

[28] R. S. Mulliken. Potential curves of diatomic rare gas molecules and their ions, with particular reference to Xe. *The Journal of Chemical Physics* **52** 5170 (1970); DOI: `10.1063/1.1672756`.

[29] A. Hitachi, T. Takahashi, N. Funayama, *et al.* Effect of ionization density on the time dependence of luminescence from liquid argon and xenon. *Physical Review B (Condensed Matter)* **27** 5279, (1983); DOI: `10.1103/PhysRevB.27.5279`.

[30] M. G. Boulay *et al.* Measurement of the scintillation time spectra and pulse-shape discrimination of low-energy β and nuclear recoils in liquid argon with DEAP-1. *Astroparticle Physics* **85** 1–23 (2016); DOI: `10.1016/j.astropartphys.2016.09.002`.

[31] F. J. Kerr and D. Lynden-Bell. Review of galactic constants. *Monthly Notices of the Royal Astronomical Society* **221** 1023-1038 (1986); DOI: `10.1093/mnras/221.4.1023`.

[32] DEAP Collaboration (M.G. Boulay). DEAP-3600 Dark Matter Search at SNOLAB. *Journal of Physics: Conference Series* 375 (2012) 012027; DOI: `10.1088/1742-6596/375/1/012027`.

[33] J. Billard, F. Mayet, D. Santos. Exclusion limits from data of directional Dark Matter detectors. *Physics Review* D **82**:055011 (2010); DOI: `10.1103/PhysRevD.82.055011`.

[34] National Institute of Standards and Technology. [Online] Available from: `http://physics.nist.gov/PhysRefData/Xcom/html/xcom1.html`.

[35] José L. Mora-Lopez. Fundamentals of Physics - Volume III, EOLSS Publications (2009), pg. 196.

[36] F. T. Avignone III. Unconventional applications of the Ge detector and the axion. *Journal of Physics: Conference Series* **173** 012015 (2009); DOI: texttt10.1088/1742-6596/173/1/012015.

[37] A. V. Derbin, I. S. Drachnev, A. S. Kayunov *et al.* Constraints on the axion-electron coupling constant for solar axions appearing owing to bremsstrahlung and the compton process. *Journal of Experimental and Theoretical Physics Letters* **95** 339 (2012); DOI: `10.1134/S002136401207003X`.

[38] G. J. Feldman, R. D. Cousins. A Unified Approach to the Classical Statistical Analysis of Small Signals. *Physics Review* D**57**, 3873 (1998); ePrint arXiv:`physics/9711021`.

[39] T. M. Karbach. Feldman-Cousins Confidence Levels - Toy MC Method. (2011); ePrint arXiv:`1109.0714`.